

Double-component convection due to different boundary conditions in an infinite slot diversely oriented to the gravity¹

N. Tsitverblit²

*Department of Fluid Mechanics and Heat Transfer, Tel-Aviv University,
Ramat-Aviv 69978, Israel*

Abstract

Onset of small-amplitude oscillatory and both small- and finite-amplitude steady double-component convection arising due to component different boundary conditions in an infinite slot is studied for various slot orientations to the gravity. The main focus is on two compensating background gradients of the components. The physical mechanisms underlying steady and oscillatory convection are analyzed from the perspective of a universally consistent understanding of the effects of different boundary conditions. In a horizontal slot with inviscid fluid addressed by Welander [Tellus, Ser. A 41 (1989) 66], oscillatory convection sets in with the most unstable wave number and oscillation frequency being zero. Exact expressions for the critical fixed-value background gradient and the respective group velocity at zero wave number are derived from the long-wavelength expansion both for the horizontal slot with independently varying background gradients and for the inclined slot with the compensating gradients. In the horizontal slot with viscous fluid, the dissipation of along-slot perturbation-cell motion reduces efficiency of the oscillatory instability feedback and thus prevents the most unstable wavelength from being infinite. Based on this interpretation, the oscillatory instability of a three-dimensional (3D) nature is predicted for an interval of long two-dimensional (2D) wavelengths in an inclined slot, and such 3D instability is indeed shown to arise. Related general conditions for three-dimensionality of most unstable disturbances are also formulated. As the slot orientation changes from the horizontal by angle θ ($\geq \pi/2$), the oscillatory 2D marginal-stability boundaries in inviscid and viscous fluid are expected to eventually transform into respective steady ones. Oscillatory instability in the vertical slot with viscous fluid, first reported by Tsitverblit [Phys. Rev. E 62 (2000) R7591], is of a quasisteady nature. Its (new) mechanism is identified. It is underlain by differential gradient diffusion. As the horizontal slot at $\theta = \pi$, addressed by Tsitverblit [Phys. Fluids 9 (1997) 2458], changes its orientation to vertical, the wave number interval of linear steady instability shrinks to the vicinity of the most unstable zero wave number and vanishes. Consistently with the basic nature of finite-amplitude steady convection being the same in the horizontal and vertical slots, the respective convective flows are continu-

ously transformed into each other. The dissimilarity between the nature of finite-amplitude steady convective flows in the horizontal slot with $\theta = 0$, revealed by Tsitverblit [Phys. Lett. A 329 (2004) 445], and that in the vertical slot is shown to eventually give rise to a region of hysteresis in $\theta \in (0, \pi/2)$.

Key words: Double-component convection, Different boundary conditions, Hydrodynamic instability

PACS: 47.20.Bp, 47.20.Ky, 47.15.Fe, 47.15.Rq

1 Introduction

This work, some of whose aspects were promulgated in [1], addresses onset of double-component, buoyancy-driven convection resulting from the boundary conditions for one component being different from those for the other. Such convection has recently been identified as a fundamentally new class of hydrodynamic instabilities underlying the formation of spatial and temporal flow patterns from a steady equilibrium state of spatially homogeneous fluid. The main emphasis of this study is on developing a universally consistent perspective for understanding the effects of different orientation of the fluid domain to the gravity.

Double-component convection is relevant to the phenomena in small-scale oceanography [2], geology [3], geodynamo [4], and such areas of astrophysics as ordinary evolution of stars [5] and core-collapse supernova explosions [6]. It has technological applications as well, in particular to crystal growth [7]. Double-component convection has also been suggested as a possible cause of layering phenomena in colloidal suspensions [8] and as the origin of pattern formation in soap films [9]. Early reviews of some of the above applications of the effects of different component diffusivities in double-component convection can be found in [10].

In addition, convective flows are commonly used in fundamental studies of

¹ NOTICE: this is the author's version of a work that was accepted for publication in Annals of Physics. Changes resulting from the publishing process, such as peer review, editing, corrections, structural formatting, and other quality control mechanisms may not be reflected in this document. Changes may have been made to this work since it was submitted for publication. A definitive version was subsequently published in Annals of Physics [Ann. Phys. (2007) 322(8) 1727-1770]
DOI 10.1016/j.aop.2006.10.001.

² Address for correspondence: 1 Yanosh Korchak Street, apt. 6, Netanya 42495, Israel; e-mail: naftali@eng.tau.ac.il

transition to turbulence and nonlinear pattern formation [11,12]. Double-component flows where a distinction between the components comes from component different boundary conditions are also of basic significance in the context of their applications to large-scale environmental and turbulent processes. In particular, such processes are Langmuir circulations [13] and the global ocean thermohaline circulation [14,15]. Except for limited aspects of the latter context, however, two-component convection in pure fluid has been previously addressed mostly in the framework of only the effects of different diffusion coefficients [16,17,18].

Welander [19] was the first to highlight the onset of oscillatory convection resulting from an unequal effect of different boundary conditions on the component diffusion gradients in perturbed state. Such convection was demonstrated in [19] to arise in a horizontal layer of inviscid fluid with a double-component, statically stable net stratification. The instability mechanism described in [19] has later been recognized by the present author [20,21] as being conceptually analogous to that driving oscillatory convection in the diffusive regime of the classical double-diffusion [16,17]. It has also been suggested in [20,21,22] that such analogy between the effect of different boundary conditions and that of unequal diffusivities is of a generic nature. Near a boundary towards which across-slot perturbation motion is directed, the component with its boundary value fixed would have a higher perturbation gradient than the component whose boundary condition is specified in terms of the flux. The different rates of gradient diffusion resulting from such a disparity could thus trigger double-component convection analogously to the effect of unequal component diffusivities in conventional double-diffusive convection.

In terms of the analogy just described, the mechanism of steady convection under the stratification inverse to that in [19] has been shown in [20,21] to be conceptually reminiscent of the finger instability in the classical double-diffusion [16]. (The mathematical problem discussed in [20,21] also happens to describe double-component Langmuir circulations [13].) In application to two horizontal gradients, the effect of different boundary conditions was also demonstrated in [22] to apply to a laterally heated stably stratified slot (LHSSS). The latter configuration had been studied before only in the context of the classical double-diffusion [23].

The above effect of boundary conditions was also demonstrated in [24] to result in steady convection when two compensating horizontal gradients maintained by different boundary conditions are applied to a vertical layer of Boussinesq fluid at rest. In the latter configuration, however, finite-amplitude convective steady flows arise without the respective linear instability of the conduction state, as in the scenario first proposed in [25]. This is qualitatively different from the analogous problem of the classical double-diffusion [26], where the respective linear instability is concomitant of subcritical steady convection.

The finite-amplitude manifestation of convection uncovered in [24] was also found to take place under a stable vertical solute stratification. In addition, the scenario in [24] unveiled the existence of an oscillatory linear instability. It thus suggested the possibility of a new oscillatory manifestation of convection due to different boundary conditions.

Differential diffusion due to unequal perturbation gradients of the components (differential gradient diffusion [19,20,21,22,24]) is not the only process by means of which different boundary conditions can trigger convection from the state of rest. As reported in [1,27], finite-amplitude steady convection could arise well before the onset of the respective linear instability in the viscous version of the problem considered in [19]. In this case, the disparity between component stratifications resulting from finite-amplitude perturbation generates convective flows due to the feedback coming from nonlinear Rayleigh—Benard convection. Such finite-amplitude convection was found in [27] to coexist with an oscillatory linear instability in viscous fluid.

The main objective of the present study is to provide a comprehensive understanding of the manifestation of infinite-slot convection resulting from different boundary conditions for diverse slot orientations to the gravity. The central issue in achieving this objective is oscillatory small-amplitude manifestation of such convection. Resulting from this work, the understanding of this issue has required uncovering and analysis of inviscid and viscous transformations of the oscillatory instability into respective steady one. In addition, it required identification of a new physical mechanism of oscillatory instability. Such instability arises in the vertical slot with viscous fluid [24]. The key physical effects underlying transformation between the inviscid mechanism of horizontal-slot oscillatory instability in [19] and the new vertical-slot mechanism in viscous fluid are thus also described in this work. Implications of the provided interpretations, in particular for the existence of a three-dimensional oscillatory instability in an inclined slot, are analyzed as well. This study also completes the understanding of steady convection due to different boundary conditions when a horizontal slot is transformed into an inclined and vertical slot.

2 The problem formulation and solution procedures

2.1 The problem and governing equations

Let compensating gradients of the contributions of two components to the density be maintained by different boundary conditions at the walls of a slot with pure fluid whose orientation to the gravity is characterized by angle θ . This is a particular case of the problem illustrated in Fig. 1, where θ (> 0 in Fig. 1) is

the angle between the direction opposite to the gravity and that of the across-slot coordinate axis. The component gradients in Fig. 1 are represented by the Rayleigh numbers $Ra = g\alpha\Delta\bar{T}d^3/\kappa\nu$ and $Ra^s = -g\beta(\partial\bar{S}/\partial\bar{x})d^4/\kappa\nu \equiv \mu Ra$. Here, \bar{x} is the (dimensional) across-slot coordinate, d is the width of the slot, $\Delta\bar{T}$ is the (dimensional) difference between the values of temperature (standing for the component with fixed-value boundary conditions) at the boundaries with smaller and larger across-slot coordinates, $\partial\bar{S}/\partial\bar{x}$ is the boundaries-prescribed (dimensional) derivative of solute concentration (standing for the component with flux boundary conditions), α is the coefficient of thermal expansion, β is the coefficient of the density variation due to the variation of solute concentration, g is the gravitational acceleration, ν is the kinematic viscosity, and $\kappa = \kappa_T = \kappa_S$ is the diffusivity of both components. The bar means that the respective variable is dimensional. Unless explicitly stated otherwise, $Ra > 0$ and $Ra^s > 0$ as well as $\mu = 1$ are assumed.

The component diffusivities are set equal to eliminate the effects of the classical double-diffusion. The effects of different boundary conditions could thus be analyzed separately from those of unequal diffusivities. Such approach is analogous to that used in previous studies of conventional double-diffusive convection. In most such studies, the components with unequal diffusivities have not been distinguished from each other in terms of boundary conditions. As indicated in [28], equal diffusivities can in principle be experimentally modeled with two solutes. The Prandtl number would then be significantly different from the $Pr = 6.7$ specified in the caption of Fig. 1. This parameter, however, is not expected to have a qualitative effect on the results and physical interpretations reported herein. Equal diffusivities could also be interpreted as eddy transport coefficients, as in [13,15]. In this case, $Pr = 6.7$ is not outside the range of realistic values corresponding to all diffusion coefficients being of the eddy type.

The condition that the component gradients be exactly compensating ($\mu = 1$) eliminates the along-slot motion arising when the slot orientation differs from horizontal. (This condition has also been adopted in many previous studies of conventional double-diffusive convection [26,29].) In the absence of such a background flow, comparison of the results for an inclined or vertical slot with those for the horizontal slot is substantially facilitated. The same could also be said about the comparison between the viscous and inviscid problems, for the along-slot base flows would have been dissimilar in such problems. In particular, these comparisons are relevant for understanding the physics of transformation between oscillatory convection in inviscid fluid at $\theta = 0$ [19] and that in viscous fluid at $\theta = \pi/2$ [24].

The equations describing the two-dimensional (2D) problem in Fig. 1 in which

an along-slot solute stratification is also present can be written as follows:

$$\begin{aligned} \frac{\partial \zeta}{\partial \tau} + \frac{\partial \psi}{\partial x} \frac{\partial \zeta}{\partial y} - \frac{\partial \psi}{\partial y} \frac{\partial \zeta}{\partial x} &= \frac{1}{Pr} \left(\frac{\partial t}{\partial x} - \frac{\partial s}{\partial x} \right) \sin \theta - \\ \frac{1}{Pr} \left(\frac{\partial t}{\partial y} - \frac{\partial s}{\partial y} \right) \cos \theta &+ \frac{\partial^2 \zeta}{\partial x^2} + \frac{\partial^2 \zeta}{\partial y^2}, \end{aligned} \quad (1)$$

$$\zeta = \frac{\partial^2 \psi}{\partial x^2} + \frac{\partial^2 \psi}{\partial y^2}, \quad (2)$$

$$\frac{\partial t}{\partial \tau} + \frac{\partial \psi}{\partial x} \frac{\partial t}{\partial y} - \frac{\partial \psi}{\partial y} \frac{\partial t}{\partial x} = \frac{1}{Pr} \left(\frac{\partial^2 t}{\partial x^2} + \frac{\partial^2 t}{\partial y^2} \right), \quad (3)$$

$$\frac{\partial s}{\partial \tau} + \frac{\partial \psi}{\partial x} \left(\frac{\partial s}{\partial y} - Ra_S \right) - \frac{\partial \psi}{\partial y} \frac{\partial s}{\partial x} = \frac{1}{Pr} \left(\frac{\partial^2 s}{\partial x^2} + \frac{\partial^2 s}{\partial y^2} \right), \quad (4)$$

where the across-slot, u , and along-slot, v , velocities are

$$u = -\frac{\partial \psi}{\partial y}, \quad v = \frac{\partial \psi}{\partial x},$$

vorticity

$$\zeta = \frac{\partial v}{\partial x} - \frac{\partial u}{\partial y},$$

solute concentration

$$S = -Ra_S y + s,$$

temperature

$$T = \frac{T_1 + T_2}{2} + t,$$

$Pr = \nu/\kappa$ is the Prandtl number, τ is the time, $x \in (-1/2, 1/2)$, $y \in (-\lambda/2, \lambda/2)$, and $\lambda = \bar{\lambda}/d$ is the specified along-slot period.

Unless explicitly emphasized otherwise, the along-slot solute stratification, characterized by the Rayleigh number $Ra_S = g\beta|\partial \bar{S}/\partial \bar{y}|d^4/\kappa\nu$, is assumed to be zero. The formulation with $Ra_S \neq 0$ is used only for facilitating the discussion related to results in [22,24], where the problems with $Ra_S \neq 0$ have been addressed.

The above equations were considered along with the no-slip formulation of wall boundary conditions

$$\begin{aligned} \zeta &= \frac{\partial^2 \psi}{\partial x^2}, \quad \psi = 0, \quad t = \pm \frac{Ra}{2}, \\ \frac{\partial s}{\partial x} &= -\mu Ra = -Ra^s \quad (x = \mp 1/2, \quad -\lambda/2 < y < \lambda/2) \end{aligned} \quad (5)$$

and periodic boundary conditions in the along-slot direction

$$\begin{aligned}
\xi(x, \lambda/2) &= \xi(x, -\lambda/2), & \frac{\partial \xi(x, \lambda/2)}{\partial y} &= \frac{\partial \xi(x, -\lambda/2)}{\partial y} \\
(-1/2 < x < 1/2), \\
s(x, \lambda/2) &= s(x, -\lambda/2), & \frac{\partial s(x, \lambda/2)}{\partial y} &= \frac{\partial s(x, -\lambda/2)}{\partial y} \\
(-1/2 < x < 0, \quad 0 < x < 1/2), & s(0, \pm\lambda/2) &= 0,
\end{aligned} \tag{6}$$

where ξ stands for ζ , ψ , and t . As indicated in the caption of Fig. 1, $Pr = 6.7$ was used throughout the present study. As at the middle points of across-slot boundaries in (6), specification of the values of s is needed to identify the solute concentration scale and select the phase of a nontrivial flow. Technical difficulties that still exist with the employed approach will be discussed in Sec. 4.2.1.

The steady version of Eqs. (1)–(4) and boundary conditions (5) and (6) was discretized by central finite differences. The Euler–Newton and Keller [30] arclength continuation algorithms were used [22] to trace out bifurcating branches of steady convection using the Harwell MA32 Fortran routine. In all these computations, the along-slot period $\lambda = 2$ was prescribed. The grid with 33 nodes in the across-slot direction was used in the computations $[nx \times \lambda(nx + 1)]$ with $nx = 33$, as in [20,22,24,27]. Temporal behavior of the linearized version of Eqs. (1)–(4) and boundary conditions (5) and (6) was also examined, in particular near the onset of oscillatory instability of the conduction state. For this purpose, the implicit method was employed to compute time evolution of the respective linear system with time step $\delta\tau = 0.05$.

2.2 Linear stability calculations

2.2.1 Two-dimensional disturbances

With the state of rest being the background flow for $\mu = 1$, the Fourier mode of a 2D marginally unstable oscillatory perturbation with angular frequency ω and wave number k can be written as

$$[u'(x), t'(x), s'(x)]^T e^{i(\omega\tau \pm ky)} + cc. \tag{7}$$

Here $[u'(x), t'(x), s'(x)]^T$ is the Fourier-mode part depending on the across-slot coordinate alone, the prime near a flow variable denotes such part in

the perturbation of the variable. Expression (7) has been introduced into the linearized Eqs. (1)—(4) rewritten for $Ra_S = 0$ in terms of across-slot velocity u , relative temperature t , and solute concentration s . This leads to:

$$\begin{aligned} & \left(\frac{d^2}{dx^2} - k^2\right)\left(\frac{d^2}{dx^2} - k^2 - i\omega\right)\tilde{u} = \\ & \mp Ra\left[ik\frac{d}{dx}(\tilde{t} - \tilde{s})\sin\theta \pm k^2(\tilde{t} - \tilde{s})\cos\theta\right], \end{aligned} \quad (8)$$

$$\left(\frac{d^2}{dx^2} - k^2 - i\omega Pr\right)\tilde{t} = \tilde{u}, \quad (9)$$

$$\left(\frac{d^2}{dx^2} - k^2 - i\omega Pr\right)\tilde{s} = \tilde{u}, \quad (10)$$

where $\tilde{u} = -u'Pr$, $\tilde{t} = t'/Ra$, and $\tilde{s} = s'/Ra^s$ ($Ra^s = Ra$).

The variables \tilde{u} , \tilde{t} , and \tilde{s} are subject to the following set of boundary conditions:

$$\tilde{u} = \frac{d^2\tilde{u}}{dx^2} = \tilde{t} = \frac{d\tilde{s}}{dx} = 0 \quad (x = \pm 1/2) \quad (11)$$

when the boundaries are stress-free. For no-slip boundaries, the set of boundary conditions is as follows:

$$\tilde{u} = \frac{d\tilde{u}}{dx} = \tilde{t} = \frac{d\tilde{s}}{dx} = 0 \quad (x = \pm 1/2). \quad (12)$$

For finding the marginally stable values of Ra and ω , it is sufficient to consider only positive values of ω and k in one such traveling wave as (7). If $[\tilde{u}(x), \tilde{t}(x), \tilde{s}(x)]^T$ is a solution of the mode $e^{i(\omega\tau + ky)}$ version of Eqs. (8)—(10) at some Ra_c and ω_c , then the mode $e^{i(\omega\tau - ky)}$ version of these equations would be satisfied by $\pm[\tilde{u}(-x), \tilde{t}(-x), \tilde{s}(-x)]^T$ at these same Ra_c and ω_c . It is thus only the mode $e^{i(\omega\tau + ky)}$ version of linear stability equations that is hereafter implied when such equations are referred to.

For examination of the linear stability of the conduction state in inviscid fluid,

$$i\omega\left(\frac{d^2}{dx^2} - k^2\right)\tilde{u} = Ra\left[ik\frac{d}{dx}(\tilde{t} - \tilde{s})\sin\theta + k^2(\tilde{t} - \tilde{s})\cos\theta\right] \quad (13)$$

was used along with

$$\left(\frac{d^2}{dx^2} - k^2 - i\omega\right)\tilde{t} = \tilde{u} \quad (14)$$

and

$$\left(\frac{d^2}{dx^2} - k^2 - i\omega\right)\tilde{s} = \tilde{u}, \quad (15)$$

where the Rayleigh numbers are defined as $Ra = g\alpha\Delta\bar{T}d^3/\kappa^2$ and $Ra^s = -g\beta(\partial\bar{S}/\partial\bar{x})d^4/\kappa^2 = Ra$. Here ω is nondimensionalized with κ/d^2 as opposed to ν/d^2 in Eqs. (8)—(10). Although the definitions of Ra , Ra^s , and ω for inviscid fluid are different from the respective definitions for viscous fluid, the same notations are used for these parameters. It is implied below that the definitions of Ra and Ra^s as well as the time nondimensionalization scale (in ω) correspond to the type of fluid in question.

The boundary conditions for inviscid fluid are

$$\tilde{u} = \tilde{t} = \frac{d\tilde{s}}{dx} = 0 \quad (x = \pm 1/2). \quad (16)$$

The inviscid problem at $\theta = 0$ was also examined for the Ra and Ra^s being independent of each other. That is, equation

$$i\omega\left(\frac{d^2}{dx^2} - k^2\right)\tilde{u} = k^2(Ra\tilde{t} - Ra^s\tilde{s}) \quad (17)$$

was considered along with Eqs. (14) and (15) and boundary conditions (16) for specified values of Ra^s .

Eqs. (9) and (10) are first solved for $\tilde{t} - \tilde{s}$, upon which the resulting general solution is introduced into Eq. (8). The latter equation is then solved for \tilde{u} , and the general expressions for \tilde{t} and \tilde{s} are thus obtained from Eqs. (9) and (10). For a fixed k , Ra_c and ω_c are then found by searching in the Ra — ω domain for the smallest Ra at which the complex matrix resulting from the application of boundary conditions (11) or (12) to the obtained general solution is singular. The same procedure was also applied to the general solution of either Eqs. (13)—(15) or Eqs. (14), (15), and (17) along with boundary conditions (16). NAG Fortran routines were employed for this purpose.

Once $Ra_c(k_0)$ and $\omega_c(k_0)$ have been found for a given k_0 , the corresponding values of these parameters, $Ra_c(k)$ and $\omega_c(k)$, at a nearby $k = k_0 + \delta k$ can be computed by the Euler—Newton continuation method. This method was applied to the solution of equation

$$F[Ra(k), \omega(k), k] = 0, \quad (18)$$

where $F[Ra(k), \omega(k), k]$ stands for the (complex) determinant of the matrix resulting from the application of boundary conditions (11), (12), or (16) to the general solution of the respective set of differential equations. As mentioned above, such determinants were computed with the use of standard Fortran routines. Numerical differentiation was thus employed to compute the Jacobian of $\{Re[F(Ra, \omega, k)], Im[F(Ra, \omega, k)]\}^T$ (with respect to Ra and ω) and $\partial F(Ra, \omega, k)/\partial k$.

One also needs to ensure that no disconnected branches of $[Ra(k), \omega(k)]^T$ satisfying the real and imaginary parts of Eq. (18) arise for the values of Ra that are smaller than those computed by the continuation procedure. For this purpose, $Ra_c(k)$ and $\omega_c(k)$ were independently obtained for several values of k by the search in the Ra — ω domain outlined above. In this case, however, the values of k could be relatively scarcely spaced within the considered wave number interval. The results of such searches were found to be entirely consistent with those obtained by the Euler—Newton continuation.

For viscous fluid, the linear stability to steady disturbances was also considered, as $\theta \in (\pi/2, \pi)$. For this purpose, $\omega = 0$ was set in Eqs. (8)—(10) and the general solution of (resulting) equations

$$(\frac{d^2}{dx^2} - k^2)^2 \tilde{u} = -Ra[ik \frac{d}{dx}(\tilde{t} - \tilde{s}) \sin \theta + k^2(\tilde{t} - \tilde{s}) \cos \theta], \quad (19)$$

$$(\frac{d^2}{dx^2} - k^2)\tilde{t} = \tilde{u}, \quad (20)$$

and

$$(\frac{d^2}{dx^2} - k^2)\tilde{s} = \tilde{u} \quad (21)$$

was obtained analytically. Either boundary conditions (11) or (12) were then applied to this general solution and the smallest Ra , $Ra_c(k)$, at which the resulting matrix becomes singular were searched for at different k .

2.2.2 Three-dimensional disturbances

For $\theta \neq 0, \pi$, a three-dimensional (3D) structure of perturbation can generally become relevant in the linear stability analysis. This study is mainly focused on 2D disturbances, for which understanding of the basic physical effects of different boundary conditions can be most conveniently obtained. Unless explicitly stated otherwise, therefore, it is the 2D linear instability that is implied below. However, 3D disturbances were also considered: in some cases, their analysis was found to be useful for understanding the 2D results.

With the same nondimensionalization as in \tilde{u} , \tilde{t} , and \tilde{s} , the Fourier mode of a 3D disturbance is described as

$$[\tilde{u}(x), \tilde{t}(x), \tilde{s}(x)]^T e^{i(\omega\tau + k_y y + k_z z)} + cc, \quad (22)$$

where k_y and k_z are the y and z components, respectively, of the full wave number $k = (k_y^2 + k_z^2)^{1/2}$. (The z -axis is orthogonal to the x — y plane in Fig. 1 and is directed towards the reader.) Expression (22) was then introduced into the appropriately nondimensionalized, linearized 3D governing equations for viscous and inviscid fluid.

With the definition of wave number k just generalized for 3D disturbances, the marginal linear stability in viscous fluid is described by the equations formally identical to Eqs. (9) and (10) along with

$$\begin{aligned} \left(\frac{d^2}{dx^2} - k^2\right)\left(\frac{d^2}{dx^2} - k^2 - i\omega\right)\tilde{u} = & -Ra[ik_y \frac{d}{dx}(\tilde{t} - \tilde{s}) \sin \theta + \\ & k^2(\tilde{t} - \tilde{s}) \cos \theta]. \end{aligned} \quad (23)$$

Likewise, the 3D marginal stability in inviscid fluid is described by the equations formally identical to Eqs. (14) and (15) along with

$$i\omega\left(\frac{d^2}{dx^2} - k^2\right)\tilde{u} = Ra[ik_y \frac{d}{dx}(\tilde{t} - \tilde{s}) \sin \theta + k^2(\tilde{t} - \tilde{s}) \cos \theta]. \quad (24)$$

For fixed values of k_z , $Ra_c(k_y)$ and $\omega_c(k_y)$ were obtained with the same procedure as described above for 2D disturbances.

3 Oscillatory convection

3.1 General

For interpretation of the findings on oscillatory instability, only a reflectionally symmetric oscillatory perturbation is considered below. In a horizontal slot, such perturbations are often referred to as standing waves. They are then characterized by convection cells changing their sense of rotation periodically in time. As suggested by [31], both reflectionally and translationally symmetric oscillatory perturbations are expected to arise from the Hopf bifurcation in a system whose background state possesses both these symmetries. Translationally symmetric oscillatory perturbations are often referred to as traveling

waves. However, it is sufficient to understand the physical mechanism of such oscillatory instability in terms of only one of the types of perturbation just mentioned. Amplitude growth of the oscillatory perturbation of the other type can then be viewed merely as a mathematical consequence of the respective results in [31].

3.2 *Inviscid fluid*

3.2.1 *Effect of the across-slot gravity.*

Let us first consider the problem in a horizontal slot addressed in [19] ($\theta = 0$), whose linear stability is described by Eqs. (14), (15), and (17) and boundary conditions (16). The marginal-stability curves, $Ra_c(k)$ and $\omega_c(k)$, are illustrated in Fig. 2. They exhibit two basic features. The first is that the most unstable wave number is zero for any Ra^s . This wave number is also characterized by zero oscillation frequency. The second feature is the existence of a minimal horizontal wavelength, decreasing with the increase of Ra^s , below which the instability does not arise.

Reinterpreting [19], rotation of a small-amplitude perturbation cell generates a potential energy of component perturbation stratifications in the end of a rotation cycle. Due to differential gradient diffusion, this potential energy is utilized by the perturbation cell in the beginning of the cycle of cell rotation in the opposite sense. The maximal amount of such energy depends on the time available for a fluid element of the cell to change its vertical coordinate. This time is specified by the horizontal scale of the instability. For this reason, $Ra_c(k)$ decreases with the increase of the horizontal wavelength and assumes its minimal value for a given Ra^s as $k \rightarrow 0$ (i.e., as wavelength $\lambda \rightarrow \infty$).

Below a certain critical wavelength, the potential energy utilized by a perturbation cell becomes insufficient for bringing about growth of the perturbation amplitude. The increase of Ra^s and associated growth of Ra_c enhance the disparity between the respective gradients in the perturbed state. This makes the energy transfer to the perturbation cells more intensive. The minimal unstable wavelength thus decreases as Ra^s grows (Fig. 2).

Efficiency of the utilization of the potential energy by a perturbation cell depends on the frequency with which the marginally unstable cells change their sense of rotation. This frequency thus has to be such that the time for vertical diffusion naturally specified by the instability wavelength be resonantly matched. Since such time grows with the wavelength increase, $\omega_c(k) \rightarrow 0$ as $k \rightarrow 0$ and $\omega_c(k)$ grows with the increase of k from 0. As the wave number is further increased, the wavelength time for the manifestation of differential diffusion eventually becomes insufficient for the cell oscillation amplitude to

grow. As a consequence, $\omega_c(k)$ begins to decrease when certain values of k are exceeded (Fig. 2), to afford more time for the diffusion.

The decrease of $\omega_c(k)$, however, leads to an inconsistency between the diffusion time afforded by the perturbation frequency and that specified by the instability wavelength. This results in the efficiency of utilization of the component potential energy by a perturbation cell being reduced. The additional energy that can actually be utilized due to such frequency decrease is thus expected to be limited. As the wave number exceeds a critical value, therefore, the instability fails to develop.

The fact that the most unstable wave number is zero makes the determination of exact values of $Ra_c(0)$ and group velocity $\omega_k^c(0) \equiv \partial\omega_c(0)/\partial k$ relevant. Also applicable to Eqs. (13)–(15) for $\theta > 0$, the long-wavelength expansion used for this purpose is as follows:

$$\begin{aligned} Ra_c(k) &= Ra_0 + k^2 Ra_2 + \dots, \\ \omega_c(k) &= k(\omega_0 + k^2 \omega_2 + \dots), \\ \tilde{u}(k) &= k(\tilde{u}_0 + k\tilde{u}_1 + k^2 \tilde{u}_2 + \dots), \\ \tilde{t}(k) &= \tilde{t}_0 + k\tilde{t}_1 + k^2 \tilde{t}_2 + \dots, \\ \tilde{s}(k) &= \tilde{s}_0 + k\tilde{s}_1 + k^2 \tilde{s}_2 + \dots \end{aligned} \tag{25}$$

Upon introduction of (25) into Eqs. (14), (15), and (17), and use of boundary conditions (16), \tilde{t}_0 , \tilde{s}_0 , and \tilde{u}_0 are first obtained. The k^1 order of Eq. (15) and the flux-free boundary conditions for \tilde{s}_1 from (16) then yield

$$\omega_k^c(0) \equiv \frac{\partial\omega_c(0)}{\partial k} = \omega_0 = \sqrt{Ra^s/12}. \tag{26}$$

Having derived the expressions for \tilde{s}_1 and \tilde{t}_1 and on introduction of these into the k^1 order of Eq. (17), one obtains the expression for \tilde{u}_1 . With such \tilde{u}_1 , the k^2 order of Eq. (15) and the flux-free boundary conditions for \tilde{s}_2 from (16) thus yield

$$Ra_c(0) = Ra_0 = (2Ra^s + 5040)/51. \tag{27}$$

The numerical data underlying the marginal-stability curves in Fig. 2 were found to accurately coincide with Eqs. (26) and (27). For the case of two compensating gradients this work is aimed at, $Ra_c(0) = Ra^s$,

$$Ra_c(0) = Ra_0 = 12 \cdot 60/7, \quad \omega_k^c(0) = \omega_0 = \sqrt{60/7}. \tag{28}$$

3.2.2 Effect of the along-slot gravity.

For the horizontal and inclined slots with two compensating across-slot gradients, $Ra_c(k)$ and $\omega_c(k)$, obtained from Eqs. (13)—(15) and boundary conditions (16), are shown in Fig. 3. (In this Sec. 3.2.2, $k_z = 0$ and thus also $k = k_y$ are implied.) As in the horizontal slot [Figs. 2 and 3(a)], $k = 0$ remains the most unstable wave number up to the orientation of the slot being nearly vertical [Figs. 3(b)—3(e)]. With increasing θ , however, $Ra_c(k)$ and $\omega_c(k)$ mostly decrease and qualitative changes arise in the shape of these curves [Figs. 3(e) and 3(f)]. This suggests the emergence of an additional factor destabilizing the system.

As suggested by [20,21], if $\theta = 0$ a viscous fluid in the region of $Ra < 0$ is expected to develop a steady instability whose mechanism is conceptually analogous to the finger instability in the classical double-diffusion [16]. Such mechanism is the only cause of linear steady instability for $0 < \theta < \pi/2$ as well (see Sec. 4.1.1 below). This steady instability would thus have finite negative values of the marginally unstable Rayleigh number for viscous fluid [21] (see also Sec. 4.1.2). Eqs. (19)—(21) then suggest that in the inviscid fluid ($Pr \rightarrow 0$), $Ra_c(k) = 0$ for the respective wave number interval. $Ra < 0$ would thus be the unstable region, with the instability mechanism being similar to that discussed in [20,21]. $Ra > 0$ is therefore the region of stability to the effect of the across-slot gravity component on steady disturbances.

As the along-slot gravity component arises with θ growing from 0, however, another mechanism of differential gradient diffusion becomes increasingly relevant. This mechanism favors a monotonic growth of disturbances. For viscous fluid, it has been discussed in [22,24]. In the absence of dissipation (throughout this work, this term implies only viscous dissipation), such mechanism is reasonably expected to be effective for small-amplitude disturbances at any $Ra \neq 0$. (The results in Fig. 3 discussed just below confirm this assumption.) So long as $\theta < \pi/2$, however, it should not give rise to steady linear instability for $Ra > 0$. The differential diffusion due to the across-slot gravity component opposes amplitude growth of the perturbation cells whose sense of rotation does not change (Sec. 3.2.1).

For $0 < \theta < \pi/2$, part of the rotation energy of a perturbation cell thus comes from the energy directly contributed via the along-slot gravity component in the current cycle of rotation [22,24]. In the end of a cell rotation cycle, the whole rotation energy is transformed into the potential energy of the perturbation stratification due to the across-slot gravity component. This potential energy is released in the next rotation cycle. Depending on the relative roles of the across-slot and along-slot gravity components, $\omega_c(k)$ thus decrease with increasing θ .

For $Ra \cos \theta$ being between 0 and the $Ra_c(k)$ from Fig. 3(a), the growth of oscillatory perturbations is largely due to the monotonic contribution of the along-slot gravity component, effective at any $Ra \neq 0$. The relative role of the across-slot gravity component in such growth on a given wavelength is specified by the respective effectiveness of transformation of the energy of cell rotation into the potential energy of the across-slot perturbation stratification. (Such process maintains the oscillatory nature of the instability.) This effectiveness can be judged based on the behavior of $Ra_c(k)$ in Fig. 3(a).

Compared to the vicinity of the infinite wavelength, finite wavelengths are less effective in transforming the energy of cell rotation into the above potential energy. This makes the relative role of the along-slot gravity component on such finite scales more pronounced than for the longer wavelengths. [As θ grows from 0 in Figs. 3(a)—3(d), in particular, $Ra_c(k)$ decrease for $k > \sim 1.1$ and, due to the decrease of the across-slot gravity component, increase slightly for $k < \sim 1$.] Near $\theta = \pi/2$, a set of finite wavelengths thus becomes more unstable than the vicinity of the infinite wavelength [Fig. 3(f)].

With the across-slot gravity component vanishing as $\theta \rightarrow \pi/2$ [Figs. 3(e) and 3(f)], however, both $Ra_c(k)$ and $\omega_c(k)$ decrease for all k . For $\theta > \pi/2$, therefore, the slot with inviscid fluid is expected to be unstable to a continuum of the wavelengths of steady disturbances for any $Ra > 0$, and it ought to be unstable for any $Ra \neq 0$ at $\theta = \pi/2$. As mentioned above, this would be consistent with the interpretations in [22,24] if the absence of dissipation is allowed for. The oscillatory and steady instabilities due to the respective effects of differential gradient diffusion in inviscid fluid are thus continuously transformed into each other around $\theta = \pi/2$.

Upon introduction of (25) into Eqs. (13)—(15), the k^1 order of these equations and boundary conditions (16) yields

$$Ra_0^2 \sin^2 \theta + 720 Ra_0 \cos \theta - 8640 \omega_0^2 = 0, \quad (29)$$

which is consistent with (26) for $\theta = 0$. The values of $Ra_c(0) = Ra_0$ and $\omega_k^c(0) = \omega_0$ estimated from the numerical data underlying the (2D) marginal-stability curves in Fig. 3 were found to be consistent with Eq. (29) to a fairly high accuracy.

3.3 Viscous fluid

3.3.1 Effect of the across-slot gravity.

The curves of 2D marginal stability for viscous fluid under stress-free and no-slip boundary conditions are illustrated in Figs. 4 and 5. They were obtained from Eqs. (8)–(10) and boundary conditions (11) and (12), respectively. (In this Sec. 3.3.1, $k_z = 0$ and thus also $k = k_y$ are implied.) The most prominent feature of the 2D curves in Figs. 4 and 5, compared to the above results for inviscid fluid, is that $k = 0$ is not the most unstable wave number and $\omega_c(k) > 0$ as $k \rightarrow 0$.

In the context of the effect of the across-slot gravity component, the obtained stability of the infinite wavelength may at first sight appear to be counterintuitive. The overall dissipation of perturbation motion is minimized when the wavelength becomes infinite. Since the effect of differential gradient diffusion is maximized for $\lambda \rightarrow \infty$, one may think that the infinite wavelength has to remain most unstable in viscous fluid as well. In particular, $k = 0$ is most unstable to steady disturbances in the viscous fluid problem identified by $\theta = \pi$ and $Ra > 0$ [20,21,32].

The relative stabilization of the long wavelengths [seen in Figs. 4(a) and 5(a), for example] with respect to the action of the across-slot gravity component is associated with a special feature of the effect of dissipation. This feature arises when the instability is oscillatory. Before describing such feature, however, it is worth illustrating details of the oscillatory instability mechanism in the horizontal slot.

Fig. 6(a) represents the stage when the previously accumulated potential energy of perturbation stratification is released after the sense of cell rotation has changed. At this stage, cell motion is favored and opposed by the horizontal solute and temperature perturbation gradients, respectively. Due to differential (across-slot) gradient diffusion, the temperature opposition to convective motion in Fig. 6(a) is overcome. Such motion thus intensifies [see ψ in Figs. 6(a) and 6(b)].

At the current stage of the oscillation period, the release of the accumulated potential energy is effected via a mechanism similar to that discussed in [20,21], where an inversely stratified problem was considered. This is particularly apparent as one compares the present Fig. 6(a) with Fig. 2(a) in [21]. In the present problem, however, the intensification of convective motion [ψ in Figs. 6(a) and 6(b)] is inevitably accompanied by changing distributions of the component perturbation isolines [s and t in Fig. 6(b)]. With the lower background values of the components at the upper wall, the clockwise (counterclockwise) rotation gives rise to the relatively smaller respective perturbations in the

right (left) part of a rotating cell. The component perturbation isolines are thus gradually reset so that cell motion be favored and opposed by the temperature and solute perturbation stratifications, respectively [Fig. 6(c)].

Due to the interaction of a rotating perturbation cell with flux boundary conditions, the solute perturbation isolines become more and more vertically oriented, in contrast to the perturbation isotherms [s and t in Figs. 6(d) and 6(e)]. The resulting differential gradient diffusion acts against the sense of rotation of a convective cell. This damps cellular motion [Figs. 6(c)—6(e)]. The energy of cell rotation is thus transformed into the potential energy of the component perturbation stratifications. Such potential energy is released [Figs. 6(f) and 6(g)] after the sense of cell rotation has changed.

The events in Figs. 6(f)—6(j) are thus qualitatively identical (up to the inverse perturbation sign) to those in Figs. 6(a)—6(e). The streamline pattern in Fig. 6(j) is different from that in Fig. 6(e). This is associated with the stages of the change in the sense of cell rotation being slightly different in these figures. Fig. 6(j) thus shows that the change of rotation sense is initiated via the formation of small cells of the opposite sense of rotation near the boundaries, where differential gradient diffusion is most effective.

The oscillatory instability thus arises when the potential energy generated during the rotation of a perturbation cell in one sense is sufficient to increase the cell amplitude while the energy is released. The release of potential energy is effected via differential gradient diffusion during the cell rotation in the opposite sense. Part of such energy, however, is inevitably spent on dissipation of along-slot cell motion. This part is the greater the larger the wavelength is. Efficiency of the (oscillatory instability) feedback is thus reduced by the dissipation. [Such feedback forms between the perturbation gradient disparity in one cycle of cell rotation and the amplitude of rotation (giving rise to such a disparity) in the next cycle.] The feedback efficiency, therefore, also tends to zero when the wavelength becomes infinite.

Although increase of the instability wavelength decreases the overall dissipation, it enhances the role of the unchanged part of the dissipation (i.e., of the dissipation of along-slot cell motion) in the oscillatory instability feedback. For sufficiently long wavelengths, the latter factor dominates the overall effect of dissipation. To avoid the zero feedback efficiency when $\omega_c \rightarrow 0$, $\omega_c(k)$ thus remains greater than zero as $k \rightarrow 0$. In the long-wavelength limit, therefore, an increasing portion of fluid particles undergoing a cycle of differential gradient diffusion fail to acquire a sufficient potential energy for their perturbation amplitude to grow in the next cycle. In the context of the effect of the across-slot gravity component, this explains the relative stabilization of long (2D) wavelengths in Figs. 4(a)—4(d) and 5(a)—5(d) compared to the respective inviscid-fluid problems [Figs. 3(a)—3(d)].

3.3.2 3D effects.

The above interpretation of the effect of viscous forces on the oscillatory instability suggests that three-dimensionality of the disturbances might be relevant in an inclined slot with viscous fluid. Let the 2D perturbation wavelength, λ_y , be large enough for the effect of dissipation on efficiency of the instability feedback to dominate the overall effect of dissipation. Such efficiency increases as the orientation of the axis of rotation of a convective cell changes and the total wavelength decreases with the emergence of a z component of the wave number: $\lambda = 2\pi/(k_y^2 + k_z^2)^{1/2} < \lambda_y = 2\pi/k_y$. The critical Rayleigh number could thus decrease compared to the 2D problem.

The horizontal-slot linear stability problem depends only on the wave number modulus. This implies that

$$Ra_c(k_y, k_z) = Ra_c[(k_y^2 + k_z^2)^{1/2}, 0]. \quad (30)$$

Let $k_y (> 0)$ be fixed, with respect to the selected coordinate system, in the interval where $Ra_c(k_y)|_{k_z=0}$ decreases with increasing k_y . Then $Ra_c(k_y)|_{k_z>0} < Ra_c(k_y)|_{k_z=0}$ for some $k_z > 0$. That $Ra_c(k_y)|_{k_z>0} > Ra_c(k_y)|_{k_z=0}$ for all positive k_y and k_z in inviscid fluid also follows from the $Ra_c(k_y)$ in Fig. 3(a) only growing with increasing k_y .

When $\theta > 0$, the wave number orientation becomes physically meaningful. For small $\theta > 0$, however, $Ra_c(k_y)|_{k_z \geq 0}$ are still largely determined by the linear stability equations for $\theta = 0$. These describe the zero-order perturbation expansion in θ of such equations for $\theta > 0$. When θ is small, therefore, most unstable disturbances with small k_y are still expected to be of 3D and 2D nature in viscous and inviscid fluid, respectively.

Such a three-dimensionality of instability hinges on the existence of an interval of growing k with decreasing $Ra_c(k)$ in a parametrically close system of marginal-stability equations for which Eq. (30) holds. It could thus also apply to different problems, where such formal conditions for the respective stability parameter are met due to other physical effects.

For a finite $\theta > 0$, the role of 3D disturbances is no longer formally predictable. However, the above physical interpretation of the effect of dissipation on the instability feedback still suggests the 3D nature of the most unstable disturbances with relatively small k_y . This effect is also due to the across-slot gravity alone. It therefore has to vanish as the slot orientation approaches vertical.

Examination of 3D oscillatory disturbances in the inviscid fluid [Figs. 3(b)—3(e)] shows that the disturbances with k_z up to 3 are more stable than the respective 2D perturbations ($k_z = 0$). Meaning that small-amplitude 3D dis-

turbances of any physical nature are not expected to arise in the range of parameters considered in Figs. 3(b)—3(e), this result is consistent with the interpretation just mentioned.

As also anticipated from the above interpretation, 3D oscillatory disturbances are most unstable in viscous fluid for an interval of k_y adjoining $k_y = 0$ [Figs. 4(b)—4(e) and 5(b)—5(e)]. In addition, the data in Figs. 4(b)—4(e) and 5(b)—5(e) indicate that 3D disturbances are the first to arise only when the across-slot gravity is present. [2D disturbances ($k_z = 0$) are most unstable for all k_y presented in Figs. 4(e) and 5(e).] Consistent with the above interpretation of the effect of the across-slot gravity component, Figs. 4(e) and 5(e) thus also suggest that the along-slot component does not introduce an additional 3D oscillatory instability.

3.3.3 Effect of the along-slot gravity.

3.3.3.1 General. As the results in Figs. 4(e) and 5(e), apart from the respective findings in [24], suggest, 2D oscillatory instability also arises due to the effect of the along-slot gravity component alone. The mechanism of such instability can be identified by careful examination of Fig. 7. In this figure, temporal behavior of an unstable perturbation mode possessing one of the reflectional symmetries of the linearized problem is illustrated.

The perturbation flow structures illustrated in Fig. 7 suggest that their dynamics is underlain by two counter-propagating patterns. Either such pattern is dominant near one of the slot sidewalls. The pattern propagating in (against) the gravity direction, i.e. downwards (upwards), is dominant near the left (right) sidewall in Fig. 7. This could be viewed as manifestation of such a perturbation being a superposition of two counter-propagating traveling waves. In particular, let $q(\tau, x, y)$ stand for the reflectionally symmetric perturbation of ψ , t , and s , nondimensionalized say consistently with Eqs. (1)—(4). If $Ra_c(k) < Ra_c(nk)$ ($n = 2, 3, \dots$), in the large- τ marginally unstable state of such a wave number k ,

$$\begin{aligned} q(\tau, x, y) &= Re[a_1^q q'(x)e^{i(\omega_c \tau + ky)} + a_2^q q'(-x)e^{i(\omega_c \tau - ky)}] \\ &= Re\{a_1^q q'(x)e^{i(\omega_c \tau + ky)}[1 + \frac{a_2^q q'(-x)}{a_1^q q'(x)}e^{-2iky}]\} \\ &= Re\{a_2^q q'(-x)e^{i(\omega_c \tau - ky)}[1 + \frac{a_1^q q'(x)}{a_2^q q'(-x)}e^{2iky}]\}. \end{aligned} \quad (31)$$

Here coefficients a_1^q and a_2^q specify the symmetry of the respective variable, and $q'(x)$ is the part of the Fourier mode of the variable depending on x alone. It

is seen from Eq. (31) that when $|q'(x)| \ll |q'(-x)|$ for $x > 0$, the slot half near the left (right) sidewall is dominated by the downwards-(upwards-)propagating traveling wave. Dynamics of such a reflectionally symmetric mode restricted to a slot half is thus largely due to the dominant part of the respective propagating pattern.

Such dominant parts of the downwards- and upwards-propagating streamline perturbation patterns are distinguishable as the along-slot sequences of counter-rotating cells in the left and right halves, respectively, of Figs. 7(d) and 7(i). Near the left (right) sidewall, the regions of the clockwise-rotating cells from such along-slot cell sequence are seen from Fig. 7 to propagate downwards (upwards) concurrently with mostly negative (positive) perturbation values of both components. The regions of such counterclockwise-rotating cells are also seen to propagate downwards (upwards) concurrently with mostly positive (negative) component perturbation values. Why such component perturbation distributions take place is analyzed below.

3.3.3.2 Component perturbation distributions. Let us consider the dominant part of either traveling streamline perturbation pattern [Figs. 7(d) and 7(i)] in the respective frame of reference moving with it. In the reference frame moving with the downwards-(upwards-)propagating pattern, the laboratory-frame velocities (Fig. 7) oriented downwards (upwards) decrease. Such velocities oriented upwards (downwards) thus increase. For an adequate speed of propagation, the component perturbations are therefore transported vertically only against the direction of propagation of the respective pattern.

The distributions of temperature and solute perturbations in Figs. 7(d) and 7(i), in particular, are in part the result of the vertical transport just highlighted. They are also due to the advection associated with across-slot laboratory-frame velocities. The orientation of such an advection is the result of addition of the along-slot component of motion against the respective direction of propagation to these laboratory-frame velocities.

Allowing for the along-slot periodicity, the regions near the upper and lower domain boundaries in Fig. 7(d) are in the wake of the downwards-propagating clockwise-rotating cells. Such a cell is seen in the left central part of the flow domain in this figure. These regions are also in the wake of the upwards-propagating counterclockwise-rotating cells represented by such cell in the right central part of the flow domain [Fig. 7(d)]. The component perturbations are thus transported into the upper- and lower-boundary regions by the velocities whose (laboratory-frame) orientation in such convective cells is against the respective direction of propagation.

The component perturbations in the upper- and lower-boundary regions in

Fig. 7(d) are also affected via the advection caused by (laboratory-frame) across-slot velocities. On addition of the along-slot component of motion against the respective direction of propagation, such across-slot velocities in the left (right) half of the slot are relevant only where they are oriented in Fig. 7(d) from (towards) the respective sidewall.

In all transport processes just outlined, the temperature and solute perturbations are transferred into the upper- and lower-boundary regions [Fig. 7(d)] only from the near-left-wall and middle areas of the slot. In such areas, the background values of the components are in the upper half of their interval.

The central region in Fig. 7(d), occupied by the full counter-rotating cells, is also in the wake of two counter-propagating convective cells. One of these is the upwards-propagating clockwise-rotating cell partly seen in the right upper corner of the domain in Fig. 7(d). The other is the downwards-propagating counterclockwise-rotating cell partly seen in the left lower corner of the domain. The component perturbations are thus transported into the central region of the domain in Fig. 7(d) by the velocities whose (laboratory-frame) orientation in such convective cells is against the respective direction of propagation. Advection due to the (laboratory-frame) across-slot velocities just below (above) the domain central region in the left (right) slot half in Fig. 7(d) also affects the component perturbations in this region.

In all transport processes just outlined, the temperature and solute perturbations are transferred into the central region of the domain in Fig. 7(d) only from the near-right-wall and middle areas of the slot. In such areas, the background values of the components are in the lower half of their interval.

The central region of the domain in Fig. 7(d) is thus characterized by the relatively smaller values of the component perturbations while the larger values are in the upper and lower regions of the domain. The dominant parts of counter-propagating streamline perturbation patterns distinguished in Fig. 7(i) are about half of the wavelength ahead of their locations in Fig. 7(d) in the respective directions. The component perturbation distributions in Fig. 7(i) are consistent with the above understanding [described for Fig. 7(d)] of the transport processes given rise to by the cells in this figure.

The component perturbations in Fig. 7(i) can also be viewed as resulting from their dominant parts being about half of the wavelength ahead of their locations in Fig. 7(d) in the respective directions. These dominant parts are however indistinguishable in Figs. 7(d) and 7(i), where they merge into the respective slot-wide patterns of the component perturbations. They are only approximately discernible in Figs. 7(a) and 7(e).

As co-rotating cells in the dominant parts of two counter-propagating streamline perturbation patterns [Figs. 7(d) and 7(i)] have close vertical locations,

they merge into a single slot-wide cell. This is seen in Figs. 7(a)—7(c), 7(e), 7(f)—7(h), and 7(j). The temperature and solute perturbations in these figures result from superposition of their respective counter-propagating perturbation patterns [whose dominant parts are roughly discernible in Figs. 7(a) and 7(e)]. The latter accompany the counter-propagating streamline patterns [whose dominant parts are discerned in Figs. 7(d) and 7(i)].

The component perturbation distributions in Figs. 7(a)—7(c), 7(e), 7(f)—7(h), and 7(j) are thus also consistent with the transport processes given rise to by the respective patterns of convective cells in these figures. Such processes have to be interpreted as in the above analysis of Figs. 7(d) and 7(i).

3.3.3.3 Feedback. In the pattern dominant part propagating downwards (upwards) near the left (right) sidewall, the clockwise-rotating cells thus steadily coincide with the regions of mostly negative (positive) perturbation values of the components. Such counterclockwise-rotating cells then steadily coincide with the regions of mostly positive (negative) component perturbation values [Figs. 7(d) and 7(i)]. In the vicinity of a sidewall, the perturbation isotherms are however prone to be parallel to the boundary, where the temperature perturbation vanishes. In contrast to this, the solute perturbation isolines tend to be orthogonal to the sidewalls, because of the flux-free boundary conditions.

Such disparate isoline behavior gives rise to differential gradient diffusion. As a consequence, a near-slot-middle streamline point in the downwards-(upwards-)propagating clockwise-rotating cells [Figs. 7(d) and 7(i)] is typically heavier (lighter) than the respective streamline point near the left (right) sidewall at the same vertical location. Likewise, a near-slot-middle streamline point in the downwards-(upwards-)propagating counterclockwise-rotating cells is typically lighter (heavier) than the respective streamline point near the left (right) sidewall at the same vertical location. [In particular, see Figs. 8(d) and 8(i).]

The flow perturbation structures illustrated in Fig. 7 are expected to result from superposition of the counter-propagating patterns whose dominant parts have just been described. They are all thus characterized by a horizontal density difference between two streamline points that is consistent with the sense of rotation of the respective convective cell. This can be inferred from Fig. 7 and is explicitly illustrated in Fig. 8.

In a quasisteady sense, therefore, the energy that drives small-amplitude oscillatory convection in Fig. 7 has essentially the same nature as that driving small- and finite-amplitude steady convection in [22,24]. In contrast to small-amplitude steady convection, such oscillatory convection arises for $\mu = 1$ because the oscillatory perturbation gives rise to a more favorable ratio between the maximal absolute values of the relative perturbations of the components.

This is discussed in Sec. 4.1.1 below, in the context of steady convection.

The streamline disturbance resulting from superposition of certain counter-propagating convective flow patterns thus generates such distribution of the component perturbations as favors its convective motion. For amplitude growth of such a disturbance to be maintained, however, the counter-propagation of the convective patterns also has to be sustained. This underlies the oscillatory nature of the instability.

It was assumed above that, in the marginally unstable state, the speed of streamline-pattern propagation adequately matches the laboratory-frame convective velocities oriented in the respective direction of propagation. The corresponding streamline points thus have their component perturbation values practically steady.

In the counter-propagating sequences of convective cells [Figs. 7(d) and 7(i)], practically steady values of the component perturbations arise in the near-wall regions of the counterclockwise-rotating cells. The values of component perturbations in these cell sequences also have to be practically steady in the middle slot regions of the clockwise-rotating cells. For all these regions, the laboratory-frame velocities are oriented in the direction of propagation of the respective streamline pattern. In the middle slot regions, the effects of temperature and solute perturbations on the density perturbation largely offset each other. Due to differential gradient diffusion, however, the density perturbation in the near-wall regions is specified primarily by the respective values of solute perturbation alone.

The solute (density) perturbation values in the near-wall regions of counterclockwise-rotating cells in Figs. 7(d) and 7(i) [Figs. 8(d) and 8(i)] are expected to be steadily positive and negative in the left and right parts of the slot, respectively. The time instances when such counter-propagating counterclockwise-rotating cells merge into a single counterclockwise-rotating cell are illustrated in Figs. 7(a)—7(c), 7(e), 7(f)—7(h), and 7(j). The values of solute (density) perturbation in such a slot-wide cell near the left sidewall are also always larger than those near the right sidewall (Fig. 8).

It is the steady horizontal density difference arising between two halves of the slot that sustains the counter-propagation underlying dynamics of the reflectionally symmetric disturbance. The counter-propagating convective streamline patterns thus give rise to such feedback distribution of the component perturbations as, due to differential gradient diffusion, enhances their convective motion and sustains their counter-propagation.

3.3.3.4 Marginal-stability boundaries. Differential gradient diffusion is most effective when a convective cell particle has the maximal time available at a particular wavelength to unequally change its component values while its across-slot location is changed. This time is the larger the longer the wavelength is. In order that the oscillatory instability mechanism just described be effective, such diffusion time has to be adequately matched by the time during which the wavelength is passed by either traveling perturbation pattern. The latter time specifies the marginal instability frequency. Such frequency in Figs. 4(e) and 5(e) thus decreases as the wavelength increases. (In this Sec. 3.3.3.4, $k_z = 0$ and thus also $k = k_y$ are implied.)

Dissipation of the along-slot component of perturbation motion is part of the feedback for the steady instability caused by different boundary conditions in a vertical-slot geometry (see Sec. 4.1.1 below). The efficiency of such a feedback thus has to decrease as the wavelength increases, as discussed for the horizontal-slot ($\theta = 0$) oscillatory instability feedback (Sec. 3.3.1).

In view of the vertical-slot oscillatory instability feedback being of a quasi-steady nature, its efficiency is also progressively reduced by the dissipation of along-slot perturbation motion when the wavelength increases. As in the horizontal-slot oscillatory instability, the feedback efficiency would also decrease to zero if the time available for across-slot diffusion as $\lambda \rightarrow \infty$ ($k \rightarrow 0$) were fully utilized. In the long-wavelength limit, therefore, $\omega_c(k)$ in Figs. 4(e) and 5(e) remains a finite nonzero value. However, differential gradient diffusion, being a basic ingredient of the vertical-slot oscillatory instability mechanism, would then have to progressively decrease its effectiveness as k approaches 0. This explains why $Ra_c(k)$ increase as k decreases near $k = 0$ in Figs. 4(e) and 5(e) and the (2D) marginal-stability curves in these figures [as well as those in Figs. 4(b)—4(d) and 5(b)—5(d)] remain qualitatively the same as in Figs. 4(a) and 5(a).

As θ increases above $\pi/2$, the emergence of the across-slot gravity component makes the associated mechanism of linear steady instability [20,21] potentially relevant. For a particular wavelength, the diffusion time thus has to optimally match a combination of the steady manifestation of the effect of the across-slot gravity component and the oscillatory one of the along-slot component. The marginally unstable frequency, $\omega_c(k)$, is thus generally expected to decrease as θ exceeds $\pi/2$. As the wavelength increases, however, such frequency specified by the effect of the along-slot gravity component alone progressively exceeds that corresponding to the maximal time available at the wavelength for the respective manifestation of differential gradient diffusion. This allows to avoid the overly large reduction of the feedback efficiency.

So long as the effect of the along-slot gravity component is dominant, the dissipation of along-slot perturbation motion remains of primary importance.

Intermediate and long wavelengths could not thus significantly decrease their marginally unstable frequency. For this reason, $\omega_c(k)$ decreases noticeably only in the region of relatively large k in Figs. 4(f) and 5(f), whereas it remains practically unchanged in the vicinity of $k = 0$. The intermediate and long wavelengths thus fail to substantially absorb the steady manifestation of the effect of the across-slot gravity component. It is only for the relatively large wave numbers, therefore, that $Ra_c(k)$ decrease with increasing θ . In contrast to this, the decreasing effect of the along-slot gravity component leads even to slight increases of $Ra_c(k)$ in the interval of relatively small wave numbers in Figs. 4(f) and 5(f).

With θ increasing above $\pi/2$, the decrease of the along-slot gravity component still enhances room for the growing across-slot component. The lower bound of the region of k with decreasing $Ra_c(k)$ is thus found to decrease [Figs. 4(f) and 5(f)]. Around $\theta \approx 1.5\pi/2$, however, $Ra_c(k)$ are still increasing (with increasing θ) when $k \leq \sim 2.5$ for both stress-free and no-slip boundary conditions. In particular, the development of a new minimum in the shape of $Ra_c(k)$ [Figs. 4(f) and 5(f)] is a manifestation of the opposing trends exhibited by $Ra_c(k)$ within the different parts of the interval of k .

For $\theta \approx 1.55\pi/2$, $\omega_c(k)$ in the regions of the smallest and largest values of k in Figs. 4(f) and 5(f) could not be continued into each other. Slope $|\partial\omega_c(k)/\partial k|$ also seemed to exhibit infinite increases around an interval of middle values of k . No marginally unstable curve with $\omega_c(k) > 0$ was then found within this interval of middle k . These findings suggest that at $\theta \approx (1.5\text{--}1.55)\pi/2$ the oscillatory marginal-stability boundaries in Figs. 4(f) and 5(f) begin to transform into the respective curves characterized by a zero real eigenvalue.

4 Steady convection

4.1 Linear steady instability

4.1.1 Effect of the along-slot gravity.

The vertical slot with inviscid fluid was found in Sec. 3.2.2 above to be unstable to steady infinitesimal disturbances for a continuum of wave numbers at any $Ra \neq 0$. In viscous fluid, however, dissipation of the along-slot component of perturbation-cell motion is part of the feedback for steady instability, if any, in the vertical-slot geometry. In particular, the component gradient disparity and resulting differential gradient diffusion are caused by across-slot perturbation motion. Such across-slot motion is however maintained only due to along-slot motion in the convective cell. Driven by the horizontal density differences

between respective streamline points, such along-slot cell motion arises from differential gradient diffusion [22,24], the process responsible for the feedback.

For viscous fluid, the linear steady instability of all wavelengths is thus generally less likely in a vertical-slot geometry than in the horizontal slot where the component stratification favors steady instability [20,21]. In addition, if such a vertical-slot instability does arise (as in [22], for example, where the background horizontal gradients are not exactly compensating), the long wavelengths are not expected to be most unstable. This is associated with the feedback efficiency tending to zero as $\lambda \rightarrow \infty$. As seen from Figs. 9 and 10, however, the long wavelengths are most unstable for all illustrated θ . Their instability is also most persistent as the interval of unstable wave numbers shrinks and vanishes when $\theta \rightarrow \pi/2$. Even when θ is very close to $\pi/2$, therefore, the instability could come only from the effect of the across-slot gravity component. This effect is known to result in such a long-wavelength instability [20,21,32].

The viscous manifestation of linear steady instability in a vertical-slot geometry seems to be limited to a more favorable background ratio between the opposing component gradients. Indeed, enhancement of the relative background solute scale with respect to that in a LHSSS ($Ra_S > 0$, $\mu = 0$) [24], taking place as μ increases from 0, is expected to be unfavorable for development of the LHSSS linear steady instability. In particular, the relative increase of the solute perturbation amplitude, associated with such solute scale enhancement, would result in a decrease of the horizontal density differences between respective streamline points of the perturbation pattern illustrated in Fig. 2(a) of [22]. This was confirmed in trial computations for $Ra_S = 30000$ and $\lambda = 2$.

Essentially the same findings are reported for $Ra_S = 0$ as well (Fig. 11), when μ increases from ~ 0.92 to ~ 0.98 . The streamline perturbation pattern in Fig. 11(a), which is similar to that in Fig. 2(a) of [22], could not be maintained as the relative solute perturbation amplitude grows when μ is increased towards 1. Such pattern is thus found to undergo changes [Figs. 11(b) and 11(c)]. The changed streamline pattern in Fig. 11(c), however, only enhances the unfavorable role of dissipation, which results in vanishing of the instability.

The reported analysis of linear steady instability for $Ra_S = 0$ was possible in view of the existence of a narrow interval of μ ($\sim 0.86 \leq \mu \leq \sim 0.98$) for which $\lambda = 2$ is unstable to steady infinitesimal disturbances. This interval has been uncovered in the present study. When μ is decreased below ~ 0.86 , the linear steady instability disappears. Vertical shear motion, intensifying with decreasing μ , becomes an important factor in the nature of the background flow. This prevents the small-amplitude manifestation of differential gradient diffusion. As μ exceeds ~ 0.98 , on the other hand, the ratio between the background component scales becomes insufficiently favorable for the mani-

festation of small-amplitude steady convection. This ratio matters so much because of the effect of dissipation on the instability feedback.

The quasisteady nature of oscillatory instability in the vertical-slot geometry suggests that the relative values of the component perturbations are critically important for the manifestation of such instability as well. In particular, the streamline patterns in Figs. 7(c), 7(g), and 7(h) are reminiscent of those in Fig. 11. The maximal absolute values of solute perturbation in Figs. 7(c), 7(g), and 7(h) are however smaller, compared to the respective temperature perturbation values, than those in Fig. 11. Counter-propagation of the streamline disturbance constituents prevents such disturbance from coherently maintaining the maximal absolute values of the solute perturbation exceeding those of the temperature perturbation. The dominant part of either traveling streamline perturbation pattern also interacts only with one of the sidewall boundary conditions. In contrast to this, the steady disturbance interacts with both such conditions.

4.1.2 *Effect of the across-slot gravity.*

When $Ra > 0$ and $\theta = \pi$, different boundary conditions result in steady linear instability. The mechanism of this instability [20,21] has to be entirely responsible for small-amplitude steady convection for $\theta \in (\pi/2, \pi)$ as well (Sec. 4.1.1).

At any $\theta \in (\pi/2, \pi)$ illustrated in Figs. 9 and 10, the instability is restricted to the wave numbers that are smaller than a certain critical value. From the qualitative point of view, this is consistent with enhancement of the overall dissipation by the wave number increase. However, such largest unstable wave number decreases to zero as θ approaches $\pi/2$. This does not seem to be a necessary consequence only of the vanishing of the across-slot gravity component. In addition, the increases of $Ra_c(k)$ in the vicinity of the largest unstable k for a given θ in Figs. 9 and 10 are noticeably more abrupt than one could expect from the behavior of $Ra_c(k)$ at the same k and larger θ . The behavior of $Ra_c(k)$ is thus affected by an additional stabilizing factor.

The curves in Figs. 9 and 10 are affected by the along-slot gravity component. In the presence of this gravity component, the steady perturbation maintained by the across-slot component would have to change its pattern. However, the along-slot gravity component alone fails to give rise to linear steady instability. Such perturbation change could thus be only stabilizing, for the resulting pattern would no longer be optimal with respect to the effect of the across-slot gravity component. In particular, the perturbation change could result in the across-slot cell path acquiring a slope with respect to the across-slot coordinate. This would enhance the dissipation of across-slot motion. Such

stabilizing effect is also most pronounced for small wavelengths, and its relative significance decreases as the wavelength increases.

Another feature of Figs. 9 and 10 is that the interval of unstable wave numbers is longer for no-slip boundary conditions (Fig. 10) when $1.4\pi/2 \leq \theta < \pi$. For $\pi/2 < \theta \leq 1.3\pi/2$, it is the stress-free conditions (Fig. 9) that give rise to a longer interval of unstable wave numbers. In the latter case, all unstable wavelengths are large enough for the dissipation of along-slot perturbation motion to dominate the overall dissipation. The stress-free boundary conditions thus allow to maintain a longer interval of unstable wavelengths. As the slot orientation is far enough from vertical, however, the shortest unstable wavelengths are such that the dissipation of across-slot motion becomes relevant. The respective critical component gradients are then larger for no-slip boundary conditions. This factor proves to be more important for maintaining the instability of the shortest wavelengths than the dissipation decrease due to the stress-free boundary conditions.

To obtain the dependence of $Ra_c(0)$ on θ ,

$$\begin{aligned} Ra_c(k) &= Ra_0 + Ra_2 k^2 + \dots, \\ \tilde{u}(k) &= k^2(\tilde{u}_0 + \tilde{u}_2 k^2 + \dots), \\ \tilde{t}(k) &= \tilde{t}_0 + \tilde{t}_2 k^2 + \dots, \\ \tilde{s}(k) &= \tilde{s}_0 + \tilde{s}_2 k^2 + \dots \end{aligned} \tag{32}$$

were introduced into Eqs. (19)—(21). $\tilde{t}_0 = 0$ and $\tilde{s}_0 = \text{const}$ were thus obtained from the k^0 order of Eqs. (20) and (21) and the boundary conditions for \tilde{t}_0 and \tilde{s}_0 . Such \tilde{t}_0 and \tilde{s}_0 were then introduced into the k^1 order of Eq. (19). Along with either (stress-free) boundary conditions (11) or (no-slip) boundary conditions (12), this resulted in the respective expressions for \tilde{u}_0 . With the use of these expressions, the k^2 order of Eq. (21) and the respective boundary conditions for \tilde{s}_2 lead to

$$Ra_c(0) = Ra_0 = -Ra_c^\pi / \cos \theta = Ra_c^\pi / \sin(\chi\pi/2). \tag{33}$$

Here Ra_c^π is the value $Ra_c(0)$ would take on in the horizontal slot ($\theta = \pi$): $Ra_c^\pi = 120$ for stress-free boundary conditions and $Ra_c^\pi = 720$ for the no-slip conditions [32]. Such values were first encountered in Rayleigh—Benard convection with the flux unstable gradient [33].

The derivation of Eq. (33) shows that the terms associated with the along-slot gravity component in the right-hand side of Eq. (19) have no impact on Eq. (33). This is consistent with the above interpretations that the effect of

this gravity component is not among the causes of linear steady instability for $\theta \in (\pi/2, \pi)$ and that any role of this effect vanishes as $k \rightarrow 0$. Eq. (33) was also found to accurately coincide with the numerical data underlying Figs. 9 and 10.

4.2 *Finite-amplitude steady convection*

4.2.1 *General.*

The specification of solute concentration at the middle points of the across-slot boundaries was found to numerically permit two pairs of periodic steady convective solutions arising from the conduction state. Within the selected along-slot period, one of such solution pairs is characterized at the onset of linear instability by two full counter-rotating cells. Except for the horizontal-slot geometry, the corresponding finite-amplitude solutions are generally reflectionally asymmetric. This is the result of an asymmetry between their counter-rotating cells (see Sec. 4.2.2 below).

In the other solution pair, a clockwise-(counterclockwise-)rotating cell in the center of the period interval is combined with parts of counterclockwise-(clockwise-)rotating cells near the across-slot boundaries. This pair possesses the reflection symmetry identified by $LS[\psi(-x, -y), t(-x, -y), s(-x, -y)]^T = [\psi(x, y), -t(x, y), -s(x, y)]^T$ for all θ . The eigenvectors in Fig. 11, in particular, correspond to the solutions that are LS -symmetric for the illustrated along-slot interval.

The only essential difference between the branch pairs is however the along-slot phase shift between their solutions. In particular, when linear steady instability is present for a given θ (say for $\theta = \pi$ or for $\theta = 0$ as $\mu < 1$), these solution pairs bifurcate from the conduction state at the Rayleigh numbers the difference between which is practically negligible. When the bifurcation is subcritical, the limit points are also formed at practically the same Ra . These pairs of branches can thus be viewed as standing for a single physically relevant pair of solution branches arising from the respective conduction state.

The two pairs of convective solution branches were however found to undergo dissimilar secondary steady bifurcation phenomena, as Ra or θ were varied. Such phenomena were detected by changes in the solution Jacobian sign, monitored during the continuation procedure. This dissimilarity could arise, in particular, from the different symmetries of the respective convective solutions, only one pair of which is LS -symmetric. In terms of the flow structure, however, the encountered secondary bifurcation phenomena were often found to give rise only to along-slot phase shifts of the respective convective patterns. The presence or absence of secondary steady bifurcations, and of the

instabilities associated with them, in real fluid could not thus be established with certainty in the framework of the present numerical approach.

In addition, the stability of finite-amplitude steady convective branches to oscillatory disturbances was found to depend on which of the two numerically present pairs of solutions is examined. This proved to hold even for the horizontal-slot geometry, where the flow pair with full counter-rotating cells also has a reflection symmetry.

The prescribed across-slot-boundary values of s can prevent traveling-wave disturbances from being detected in the present formulation. However, finite-amplitude traveling-wave branches could intersect steady convective branches and thus affect the stability of the latter. Such findings have been previously reported for binary fluid convection [34] and for conventional double-diffusive convection [35]. The presence of traveling-wave branches also affects the stability of reflectionally symmetric oscillatory branches [31]. This could have an additional effect on the stability of finite-amplitude steady solutions. The stability of steady convective branches to secondary oscillatory disturbances may therefore anyway change if the existence of traveling waves is properly allowed for.

The solution structures reported below thus refer to the two pairs of steady convective branches arising in such numerical computations as one, as has been done for the periodic solution computations in [22,24,27] as well. The focus of this study is also on the physical mechanisms of conduction-state instability. For the reasons just mentioned, therefore, the issues of secondary (steady and oscillatory) instability of the computed finite-amplitude steady flows were left outside the scope of this work.

4.2.2 $\theta \in [\pi/2, \pi]$.

For a large enough perturbation amplitude at $\theta = \pi/2$, an appropriate streamline pattern is maintained by the combined action of differential gradient diffusion and along-slot gravity [24]. This is possible despite the effects of dissipation, due to the energy coming from the nonlinear terms in Eqs. (1)–(4).

As θ changes from π to $\pi/2$, the mechanism of differential gradient diffusion discussed in [20,21] thus gradually gives way to that considered in [24]. Via supercritical bifurcation, the former mechanism gives rise to a convective steady pattern of symmetric counter-rotating cells. The steady convection pattern resulting from the finite-amplitude mechanism in [24] has however only clockwise-rotating cells. The along-slot gravity component has an asymmetric effect on the senses of rotation of the counter-rotating cells.

In particular, let a perturbation pattern of symmetric counter-rotating cells

be generated in a vertical slot with two background horizontal gradients and the higher component values at the left sidewall. The clockwise-rotating cells would then create locally unstable solute perturbation stratifications. Such stratifications would however be stable where the cells rotate counterclockwise. Due to differential diffusion (whether of gradient or classical nature), the clockwise-rotating cells have to intensify with respect to the cells rotating counterclockwise [22,23,24,26]. The clockwise-rotating cells are thus dominant in the finite-amplitude steady pattern.

At the onset of linear steady instability, the counter-rotating cells are bound to be symmetric. The asymmetry between them could thus arise, as θ changes from π to $\pi/2$, only with a finite convection amplitude. The latter is expected to arise when the Rayleigh number increases above the linear instability onset. The effect of the along-slot gravity component is itself also enhanced as the Rayleigh number is increased. For $Ra = 31000$ and $\lambda = 2$, in particular, the flow patterns are thus entirely dominated by the clockwise-rotating cells when θ is still greater than $1.9\pi/2$ [Figs. 12(a)—12(d)]. The remnants of the counterclockwise-rotating cells also vanish for $\theta \in (1.7\pi/2, 1.75\pi/2)$ [Figs. 12(e)—12(h)].

For $\theta \in [\pi/2, \pi]$, differential gradient diffusion underlies the convective mechanisms resulting from both the along-slot and the across-slot gravity components. The mechanism at $\theta = \pi/2$, however, leads only to nonlinear steady instability. As θ changes from π to $\pi/2$, primary control over finite-amplitude steady convection is thus continuously transformed from the convective mechanism arising from the across-slot gravity component to that associated with the along-slot component. Such linear instability can however be due to the decreasing across-slot gravity component alone. At some $\theta[\approx (1.6\text{--}1.7)\pi/2$ for $\lambda = 2]$, this renders the steady bifurcation subcritical, as seen from Figs. 13(a) and 13(b). As the across-slot gravity component further decreases with θ being decreased [to $\theta \in (1.3\pi/2, 1.4\pi/2)$ for $\lambda = 2]$, the linear steady instability vanishes [Figs. 13(c) and 13(d)].

4.2.3 $\theta \in [0, \pi/2]$.

For $\theta \in [0, \pi/2]$, linear steady instability can arise for $\mu = 1$ neither from the effect of the along-slot gravity component nor from that of the across-slot component. The latter effect favors amplitude growth only of the small-amplitude convective cells whose sense of rotation changes periodically in time (Secs. 3.2.1 and 3.3.1). In addition, differential gradient diffusion is not among the causes of finite-amplitude steady convection at $\theta = 0$. Rather, it plays only a stabilizing role in the mechanism of such convection [27].

The nature of finite-amplitude steady convective flows at $\theta = 0$ is thus ba-

sically different from that at $\theta = \pi/2$. As the convection amplitude becomes large enough, with the Rayleigh number being increased, such dissimilarity in the nature of convection prevents continuous transformation of one of the convective steady flows into the other. In particular, a region of hysteresis in θ is formed for $Ra > \sim 20000$ (Fig. 14).

As θ increases from 0, finite-amplitude steady convection at $Ra = 31000$ remains under primary control of the effect of the across-slot gravity component. Playing a stabilizing role in this effect [27], differential gradient diffusion reduces the relative significance of its destabilizing role in the emerging effect of the along-slot gravity component. The counterclockwise-rotating cells thus retain their horizontal-slot pattern along the whole branch $A2_h$ [Figs. 15(a) and 15(b)]. For $Ra = 31000$ and $\lambda = 2$, this branch extends to about $\theta \approx 0.51\pi/2$ [Fig. 14(c)].

With θ decreasing from $\pi/2$, finite-amplitude steady convection remains under primary control of the effect of the along-slot gravity component. This effect is underlain by differential gradient diffusion [22,24]. Such process reduces the effectiveness of the convective mechanism by means of which the emerging across-slot gravity component acts [27]. This gravity component thus fails to have a significant effect on the convective pattern (i.e., to generate counterclockwise-rotating cells). The whole branch $A2_v$, extending to $\theta \approx 0.38\pi/2$ for $Ra = 31000$ and $\lambda = 2$, is therefore characterized only by clockwise-rotating cells [Fig. 15(d)]. Along branch $A2_{hv}$ [Fig. 14(c)], such convection pattern is transformed into that with counter-rotating cells [Figs. 15(b) and 15(c)].

5 Summary and concluding remarks

This work provides a comprehensive understanding of the manifestation of double-component convection due to the effects of different component boundary conditions in an infinite slot having diverse orientations to the gravity. To eliminate other physical effects, the primary focus has been on the problem with compensating gradients of the components and equal component diffusivities. Small-amplitude oscillatory convection as well as small- and finite-amplitude steady convection have been considered. Although the study was primarily focused on 2D convection, small-amplitude 3D effects were also examined where the obtained physical insight suggested their potential relevance.

The main aspect of the provided understanding is a consistent interpretation of the physics underlying small-amplitude oscillatory convection. For all slot orientations, the physical nature of such convection both in inviscid and in viscous fluid proved to be underlain by differential gradient diffusion. However,

the specific mechanisms by means of which the manifestation of this effect takes place vary significantly with the slot orientation. Their features also depend substantially on whether the involved fluid is of inviscid or viscous nature.

In the horizontal slot at $\theta = 0$ with inviscid fluid and an independently prescribed flux stratification, Ra^s , the marginal-stability boundaries behave consistently with the physical mechanism of oscillatory instability first highlighted in [19]. In particular, the most unstable wave number is zero and the instability arises within a finite wave number interval. The oscillation frequency also decreases with decreasing wave number and becomes zero at $k = 0$. By means of the long-wavelength expansion, the critical fixed-value stratification, Ra_c , and the group velocity, $\partial\omega_c/\partial k$, for $k = 0$ were expressed in terms of Ra^s .

For the compensating background gradients in inviscid fluid, the most unstable wave number remains equal to zero up until the slot orientation becomes nearly vertical ($\theta = \pi/2$). The analytical relation between Ra_c and $\partial\omega_c/\partial k$ at $k = 0$ was derived for such inclined slot at any $\theta \in [0, \pi/2)$ as well. For θ growing from 0 to $\pi/2$, the oscillatory instability is however increasingly affected by the along-slot gravity component. The effect of this gravity component is associated with the mechanism of steady instability identified in [22,24] for viscous fluid. The oscillatory marginal-stability curves for $\theta \in (0, \pi/2)$ were found to behave consistently with the assumption that the corresponding mechanism in inviscid fluid is effective at any $Ra \neq 0$. In particular, the oscillatory marginal-stability boundary was found to transform into the steady one with $Ra_c(k) = 0$ as $\theta \rightarrow \pi/2$.

In the horizontal slot ($\theta = 0$) with viscous fluid, the vicinity of zero wave number is no longer the region of most unstable k . $\omega_c(k)$ also tends to a nonzero value as $k \rightarrow 0$. These findings are still consistent with the interpretation of the oscillatory instability for inviscid fluid. In particular, the dissipation of along-slot perturbation motion was found to be part of the feedback in the horizontal-slot oscillatory instability mechanism. Increase of the instability wavelength thus reduces the efficiency of such feedback. As k approaches 0, this stabilizing factor becomes more important than the destabilizing decrease of the overall dissipation.

The suggested interpretation of the role played by the dissipation of along-slot motion in the horizontal-slot oscillatory instability feedback apparently applies to the classical double-diffusion as well. In particular, zero wave number has to be most unstable in the diffusive regime of conventional double-diffusive convection when both background gradients in inviscid fluid are maintained by flux boundary conditions. Indeed, Fig. 4(b) in [36] seems to suggest that the most unstable wavelength tends to infinity and the oscillation frequency tends to zero as $Pr \rightarrow 0$. For a finite Pr , however, both the most unstable

wavelength and the corresponding oscillation frequency in Fig. 4(b) of [36] are finite.

For relatively large λ_y , most unstable disturbances of the oscillatory instability in an inclined slot [$\theta \in (0, \pi/2)$], where the across-slot gravity component is involved in driving the instability, are of a 3D nature. This was also suggested to result from the effect of dissipation of along-slot perturbation motion. In particular, the feedback efficiency increases when λ decreases due to orientation change of the 2D axis of rotation of a perturbation cell. All relevant findings proved to be consistent with such interpretation of the 3D instability nature. For small $\theta > 0$, this interpretation was also found to be a manifestation of more general conditions for three-dimensionality of instability. Such conditions were formulated independently of the physics underlying a specific problem.

Another important outcome of this study is identification of the oscillatory instability mechanism arising from the effect of the along-slot gravity component in viscous fluid. The reflectionally symmetric perturbation mode of this instability consists of two counter-propagating patterns either of which is dominant near one of the slot sidewalls. The counter-traveling convective streamline patterns give rise to such feedback distribution of the component perturbations as generates their amplitude growth and a nearly steady density difference across the slot. This density difference sustains the counter-propagation of the convective patterns. Such growth of the convection amplitude and formation of the across-slot density difference are underlain by differential gradient diffusion. In a quasisteady sense, the manifestation of such differential diffusion is analogous to that in the respective steady instability [22,24].

The identified mechanism of vertical-slot oscillatory instability is apparently also relevant under the conditions other than those considered in this work. In particular, Fig. 5 in [37] suggests that oscillatory instability arises in the vertical slot filled with a porous medium even when different boundary conditions could be the only cause of this instability. In addition, the instability mechanism identified in the present study may also be effective when the role of differential gradient diffusion in it is played by the classical double-diffusion. Indeed, the directions in which counter-propagating flow patterns travel in Fig. 8 of [37] seem to be consistent with the respective directions in Fig. 7 of the present work. The eigenfunctions of traveling waves illustrated in Fig. 7 of [37] are also dominated by their patterns near the respective slot boundaries.

The quasisteady nature of oscillatory instability in the vertical slot suggests that the dissipation of along-slot perturbation motion is part of the instability feedback, as also highlighted for the respective mechanism of steady instability. Since such a dissipation is part of the oscillatory instability feedback at $\theta = 0$ as well, the same shape of the oscillatory marginal-stability boundaries for all

$\theta \in [0, \pi/2]$ is thus explained. In contrast to small-amplitude steady vertical-slot convection, the manifestation of such quasisteady oscillatory convection is permitted due to a relatively more favorable ratio between the maximal absolute values of the component perturbations.

As θ exceeds $\pi/2$, the mechanism of linear steady instability arising from the effect of the across-slot gravity component [20,21] becomes increasingly involved in the manifestation of oscillatory instability due to the along-slot component. Behavior of the oscillatory marginal-stability curves above $\theta \approx 1.5\pi/2$ was thus found to suggest their transformation into the respective curves characterized by a zero real eigenvalue.

The effect of the across-slot gravity component identified in [20,21] is the only cause of linear steady instability for $\theta \in (\pi/2, \pi]$. Driven by differential gradient diffusion, such instability arises within a finite interval of wave numbers that extends from the most unstable zero wave number. Obtained from the long-wavelength expansion, Ra_c at $k = 0$ is not affected by the along-slot gravity component at all. However, the along-slot gravity component still has a stabilizing effect on small-amplitude steady perturbations with $k > 0$. This effect is manifested in that the interval of unstable wave numbers shrinks to the vicinity of $k = 0$ and vanishes with θ decreasing from π to $\pi/2$.

The effect of the along-slot gravity component still gives rise to finite-amplitude steady convection. In contrast to the finite-amplitude pattern of symmetric counter-rotating convective cells at $\theta = \pi$, the convection pattern at $\theta = \pi/2$ comprises only clockwise-rotating cells. Underlain by differential gradient diffusion, the basic nature of finite-amplitude convective steady flows at $\theta = \pi/2$ is however the same as that at $\theta = \pi$. Continuous transformation between these flows was thus demonstrated to take place at least up to $Ra = 31000$.

In contrast to $\theta \in [\pi/2, \pi]$, finite-amplitude convective steady flows at $\theta = 0$ could not be continuously transformed into those at $\theta = \pi/2$ for $Ra = 31000$. Rather, a region of hysteresis in θ was demonstrated to develop above $Ra \approx 20000$. Such hysteresis phenomenon is a manifestation of the basic nature of finite-amplitude steady convection at $\theta = 0$ being different from that at $\theta = \pi/2$. In particular, differential gradient diffusion is a stabilizing factor with respect to the effect of the across-slot gravity component on finite-amplitude steady convection for $\theta \in [0, \pi/2)$. It is the opposite roles of this physical process in the effects of the across-slot and along-slot gravity components that prevents continuous transformation between the finite-amplitude steady flows at $\theta = 0$ and $\theta = \pi/2$.

The reported mechanisms of double-component convection due to different component boundary conditions thus comprise two basic ingredients. These are the disparity between component stratifications caused by a convective

perturbation and the resulting feedback that maintains amplitude growth of such a perturbation. For all slot orientations, the feedback in small-amplitude oscillatory and steady convection is underlain by differential gradient diffusion. In particular, such universality of the nature of small-amplitude convection is manifested in the transformations of oscillatory marginal-stability curves into steady ones. Finite-amplitude steady convection can however arise due to two dissimilar feedbacks. The role of differential gradient diffusion is destabilizing in one of them and stabilizing in the other.

The disparity between component gradients in perturbed state is thus the only universal feature of the effects of different boundary conditions. This feature is however also independent of the physical nature of the forces responsible for the feedback. It could therefore be expected to give rise to instabilities when the forces generated by components are other than the buoyancy forces. Analysis of such possibilities could provide a further insight into the effects of different boundary conditions.

References

- [1] N. Tsitverblit, Geophys. Res. Abs. 4 (2002) CD-ROM; see also <http://www.copernicus.org/EGS/egsga/nice02/programme/overview.htm>.
- [2] R. W. Schmitt, Annu. Rev. Fluid Mech. 26 (1994) 255–285.
- [3] H. E. Huppert, R. S. J. Sparks, Annu. Rev. Earth Planet. Sci. 12 (1984) 11–37.
- [4] F. H. Busse, Geophys. Res. Lett. 29 (2002) 1105.
- [5] E. A. Spiegel, Annu. Rev. Astron. Astrophys. 10 (1972) 261–304; D. W. Hughes, M. R. E. Proctor, Annu. Rev. Fluid Mech. 20 (1988) 187–223; V. M. Canuto, Astrophys. J. 524 (1999) 311–340.
- [6] H. A. Bethe, Rev. Mod. Phys. 62 (1990) 801–866; A. Mezzacappa, Annu. Rev. Nucl. Part. Sci. 55 (2005) 467–515.
- [7] S. R. Coriell, R. F. Sekerka, PCH, PhysicoChem. Hydrodyn. 2 (1981) 281–293; C. W. Lan, Chem. Eng. Sci. 59 (2004) 1437–1457.
- [8] D. M. Mueth, J. C. Crocker, S. E. Esipov, D. G. Grier, Phys. Rev. Lett. 77 (1996) 578–581.
- [9] B. Martin, X. L. Wu, Phys. Rev. Lett. 80 (1998) 1892–1895.
- [10] J. S. Turner, Annu. Rev. Fluid Mech. 6 (1974) 37–54; *ibid.* 17 (1985) 11–44.
- [11] R. P. Behringer, Rev. Mod. Phys. 57 (1985) 657–687.
- [12] M. C. Cross, P. C. Hohenberg, Rev. Mod. Phys. 65 (1993) 851–1112; E. Bodenschatz, W. Pesch, G. Ahlers, Annu. Rev. Fluid Mech. 32 (2000) 709–778.

- [13] S. Leibovich, *Annu. Rev. Fluid Mech.* 15 (1983) 391–427; S. A. Thorpe, *ibid.* 36 (2004) 55–79.
- [14] H. Stommel, *Tellus* 13 (1961) 224–230; G. Walin, *Palaeogeogr. Palaeoclimatol. Palaeoecol.* 50 (1985) 323–332.
- [15] C. Quon, M. Ghil, *J. Fluid Mech.* 245 (1992) 449–483; H. A. Dijkstra, M. J. Molemaker, *ibid.* 331 (1997) 169–198.
- [16] M. E. Stern, *Tellus* 12 (1960) 172–175.
- [17] G. Veronis, *J. Mar. Res.* 23 (1965) 1–17; *J. Fluid Mech.* 34 (1968) 315–336; R. L. Sani, *AIChE (Am. Inst. Chem. Eng.) J.* 11 (1965) 971–980.
- [18] M. E. Stern, *Deep-Sea Res.* 14 (1967) 747–753.
- [19] P. Welander, *Tellus, Ser. A* 41 (1989) 66–72.
- [20] N. Tsitverblit, in: S. Meacham (Ed.), *Double-Diffusive Processes*, Woods Hole Oceanographic Institution, Technical Report No. WHOI-97-10, 1997, pp. 145–159.
- [21] N. Tsitverblit, *Phys. Fluids* 9 (1997) 2458–2460.
- [22] N. Tsitverblit, *Phys. Fluids* 11 (1999) 2516–2538.
- [23] S. A. Thorpe, P. K. Hutt, R. Soulsby, *J. Fluid Mech.* 38 (1969) 375–400; J. E. Hart, *ibid.* 49 (1971) 279–288; *ibid.* 59 (1973) 47–64; S. Thangam, A. Zebib, C. F. Chen, *ibid.* 112 (1981) 151–160; Y. Young, R. Rosner, *Phys. Rev. E* 57 (1998) 5554–5563; O. S. Kerr, K. Y. Tang, *J. Fluid Mech.* 392 (1999) 213–232.
- [24] N. Tsitverblit, *Phys. Rev. E* 62 (2000) R7591–R7594.
- [25] S. Rosenblat, S. H. Davis, *SIAM (Soc. Ind. Appl. Math.) J. Appl. Math.* 37 (1979) 1–19.
- [26] S. Xin, P. Le Quéré, L. S. Tuckerman, *Phys. Fluids* 10 (1998) 850–858; see also the references therein.
- [27] N. Tsitverblit, *Phys. Lett. A* 329 (2004) 445–450.
- [28] A. A. Predtechensky, W. D. McCormick, J. B. Swift, Z. Noszticzius, H. L. Swinney, *Phys. Rev. Lett.* 72 (1994) 218–221; A. A. Predtechensky, W. D. McCormick, J. B. Swift, A. G. Rossberg, H. L. Swinney, *Phys. Fluids* 6 (1994) 3923–3935.
- [29] A. Bergeon, K. Ghorayeb, A. Mojtabi, *Phys. Fluids* 11 (1999) 549–559; G. Bardan, A. Bergeon, E. Knobloch, A. Mojtabi, *Physica D* 138 (2000) 91–113; A. Bergeon, E. Knobloch, *Phys. Fluids* 14 (2002) 3233–3250.
- [30] H. B. Keller, in: P. H. Rabinowitz (Ed.), *Applications of Bifurcation Theory*, Academic, New York, 1977, pp. 359–384.
- [31] M. Golubitsky, I. Stewart, *Arch. Ration. Mech. Anal.* 87 (1985) 107–165; J. D. Crawford, E. Knobloch, *Annu. Rev. Fluid Mech.* 23 (1991) 341–387.

- [32] D. A. Nield, J. Fluid Mech. 29 (1967) 545–558; S. Leibovich, S. K. Lele, I. M. Moroz, *ibid.* 198 (1989) 471–511.
- [33] E. M. Sparrow, R. J. Goldstein, V. K. Jonsson, J. Fluid Mech. 18 (1964) 513–528; D. T. J. Hurle, E. Jakeman, E. R. Pike, Proc. R. Soc. Ser. A 296 (1967) 469–475.
- [34] W. Barten, M. Lücke, M. Kamps, R. Schmitz, Phys. Rev. E 51 (1995) 5636–5661.
- [35] A. E. Deane, E. Knobloch, J. Toomre, Phys. Rev. A 36 (1987) 2862–2869.
- [36] M. Mamou, P. Vasseur, M. Hasnaoui, J. Fluid Mech. 433 (2001) 209–250.
- [37] M. Mamou, Phys. Fluids 14 (2002) 4302–4314.

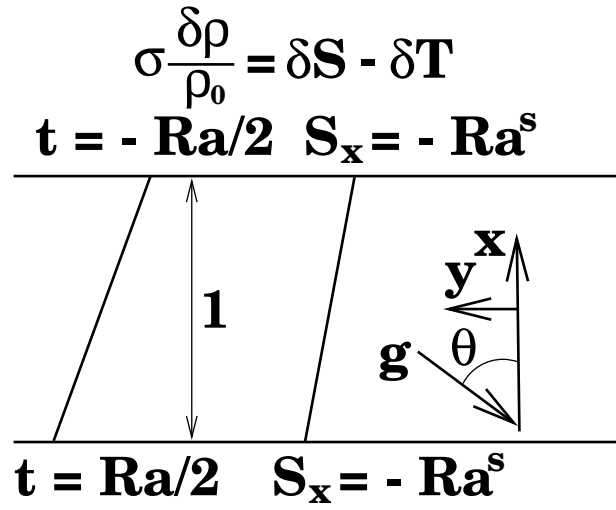


Fig. 1. Geometry of the problem. $\delta\rho = \rho - \rho_0$ is the variation of the (dimensionless) density, ρ , due to the variations δS and δT of solute concentration S and temperature $T = (T_1 + T_2)/2 + t$ with respect to their reference values, at which the density is ρ_0 ; T_1 and T_2 are the boundary temperatures, $\sigma = gd^3/\kappa\nu$. $Pr \equiv \nu/\kappa = 6.7$, $Le \equiv \kappa_T/\kappa_S = 1$; κ_T and κ_S ($= \kappa$) are the component diffusivities. The fluid is of the Boussinesq type.

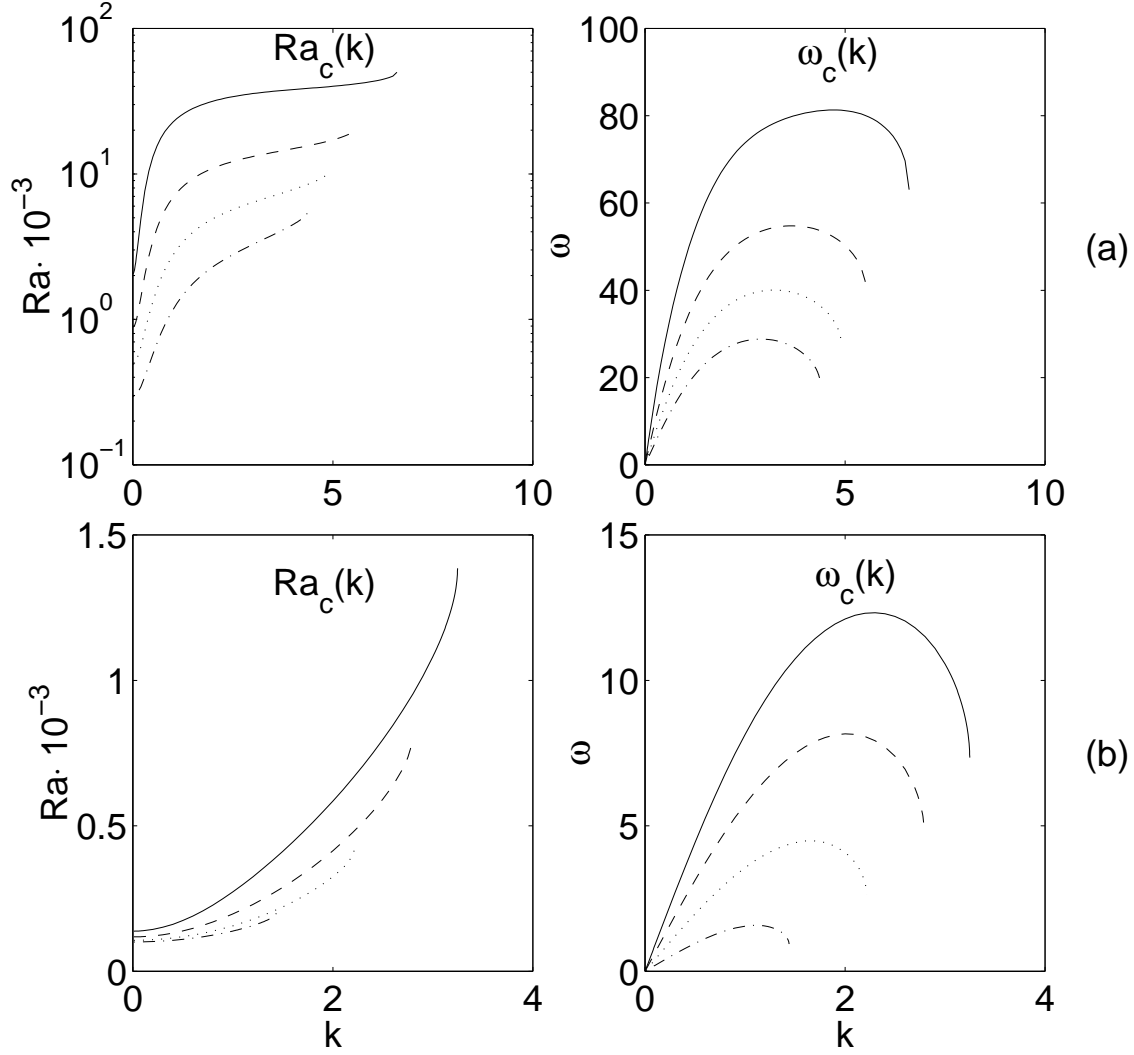


Fig. 2. $\theta = 0$. Inviscid fluid. Curves of the marginal linear stability to 2D oscillatory disturbances for independently prescribed Ra^s , $Ra_c(k)$ and $\omega_c(k)$; $Le = 1$. (a) the solid lines: $Ra^s = 50000$, the dashed lines: $Ra^s = 20000$, the dotted lines: $Ra^s = 10000$, the dash-dot lines: $Ra^s = 5000$; (b) the solid lines: $Ra^s = 1000$, the dashed lines: $Ra^s = 500$, the dotted lines: $Ra^s = 200$, the dash-dot lines: $Ra^s = 50$.

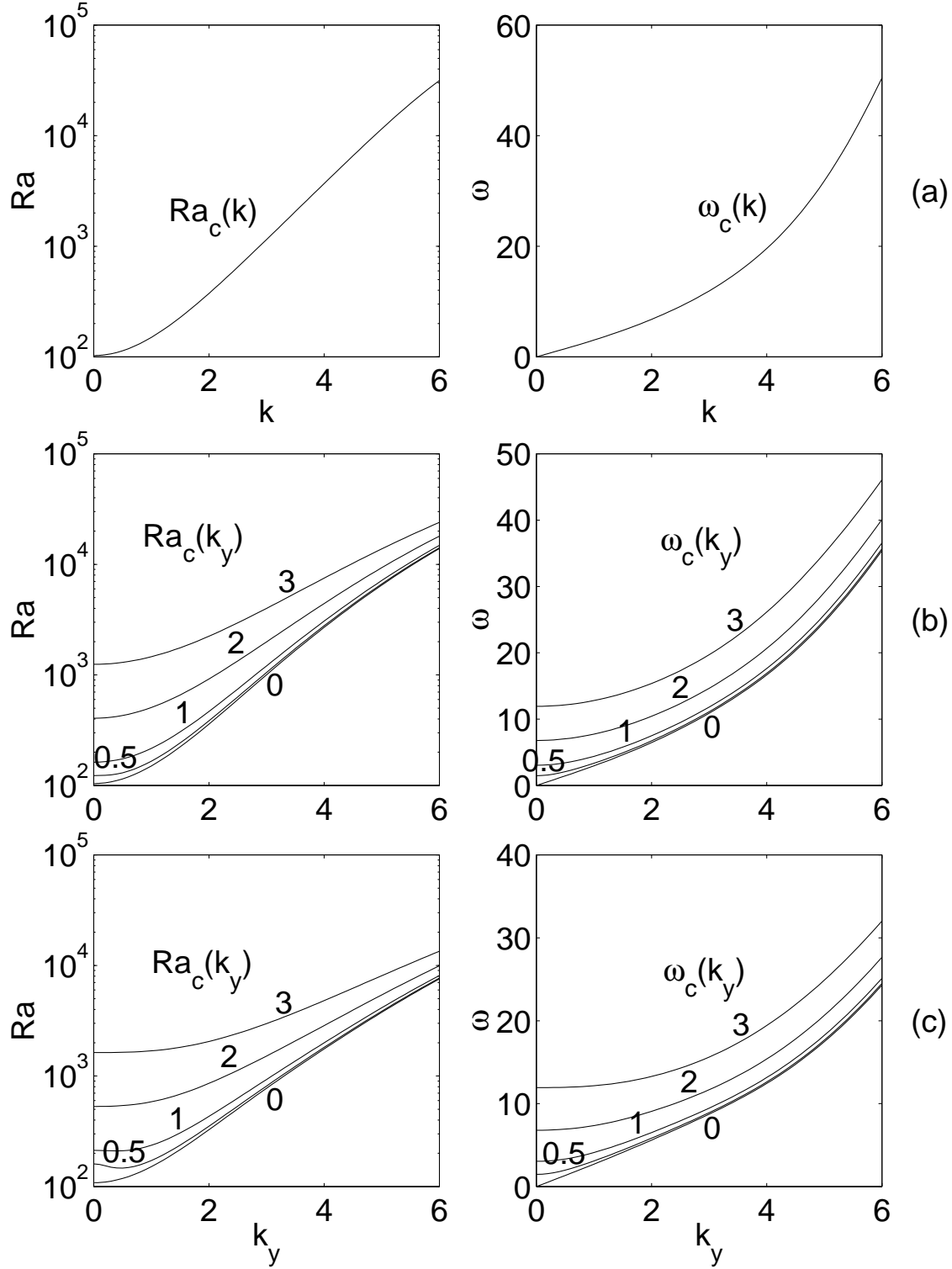


Fig. 3. Inviscid fluid. Curves of the marginal linear stability to 2D ($k_z = 0$) oscillatory disturbances, $Ra_c(k)$ and $\omega_c(k)$, and to such 3D ($k_z \geq 0$) disturbances with different values of k_z , $Ra_c(k_y)$ and $\omega_c(k_y)$; $\mu = 1$, $Le = 1$. The numbers in (b)—(e), where the disturbances with $k_z > 0$ were also considered, give the values of k_z corresponding to their nearest curve they do not intersect. (a) $\theta = 0$; (b) $\theta = \pi/8$; (c) $\theta = \pi/4$; (d) $\theta = 3\pi/8$; (e) $\theta = 0.95\pi/2$; (f) the dotted lines: $\theta = 0.99\pi/2$, the dashed lines: $\theta = 0.995\pi/2$, the solid lines: $\theta = 0.999\pi/2$.

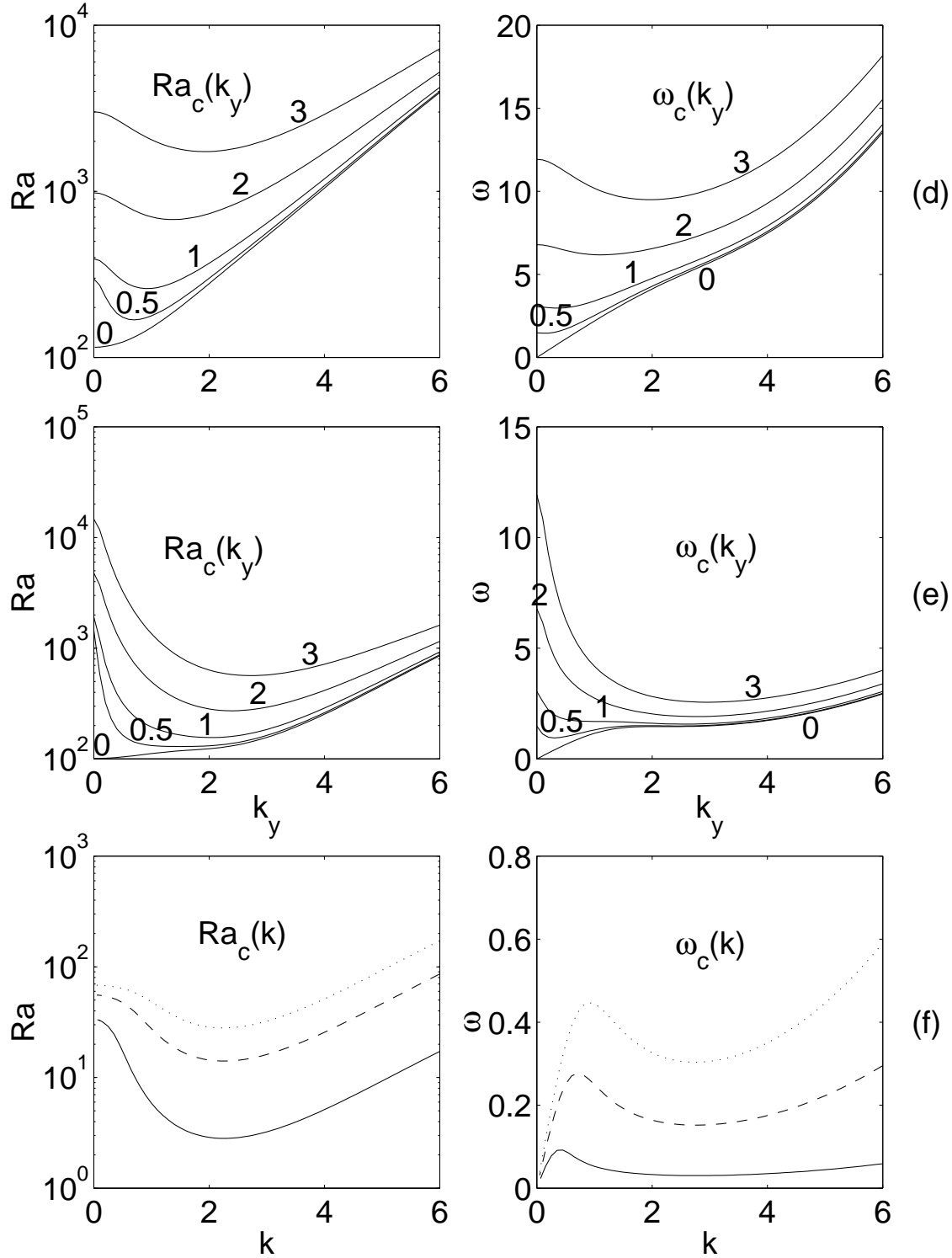


Fig. 3. Inviscid fluid. Curves of the marginal linear stability to 2D ($k_z = 0$) oscillatory disturbances, $Ra_c(k)$ and $\omega_c(k)$, and to such 3D ($k_z \geq 0$) disturbances with different values of k_z , $Ra_c(k_y)$ and $\omega_c(k_y)$; $\mu = 1$, $Le = 1$. The numbers in (b)–(e), where the disturbances with $k_z > 0$ were also considered, give the values of k_z corresponding to their nearest curve they do not intersect. (a) $\theta = 0$; (b) $\theta = \pi/8$; (c) $\theta = \pi/4$; (d) $\theta = 3\pi/8$; (e) $\theta = 0.95\pi/2$; (f) the dotted lines: $\theta = 0.99\pi/2$, the dashed lines: $\theta = 0.995\pi/2$, the solid lines: $\theta = 0.999\pi/2$.

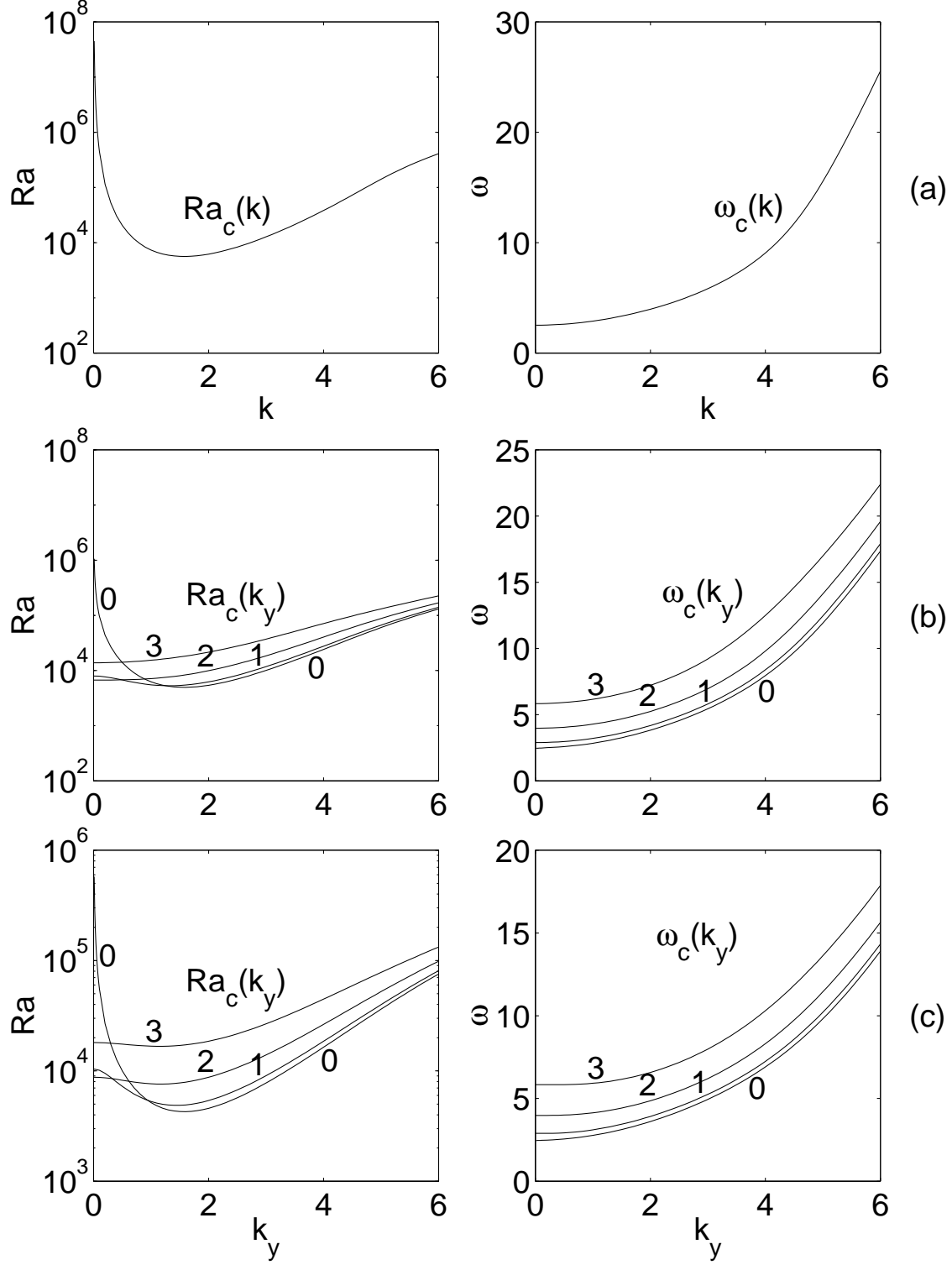


Fig. 4. Viscous fluid and stress-free slot boundaries. Curves of the marginal linear stability to 2D ($k_z = 0$) oscillatory disturbances, $Ra_c(k)$ and $\omega_c(k)$, and to such 3D ($k_z \geq 0$) disturbances with different values of k_z , $Ra_c(k_y)$ and $\omega_c(k_y)$; $\mu = 1$, $Pr = 6.7$, $Le = 1$. The numbers in (b)–(e), where the disturbances with $k_z > 0$ were also considered, give the values of k_z corresponding to their nearest curve they do not intersect. (a) $\theta = 0$; (b) $\theta = \pi/8$; (c) $\theta = \pi/4$; (d) $\theta = 3\pi/8$; (e) $\theta = \pi/2$; (f) the dash-dot lines: $\theta = 5\pi/8$, the dotted lines: $\theta = 1.35\pi/2$, the dashed lines: $\theta = 1.45\pi/2$, the solid lines: $\theta = 1.49\pi/2$.

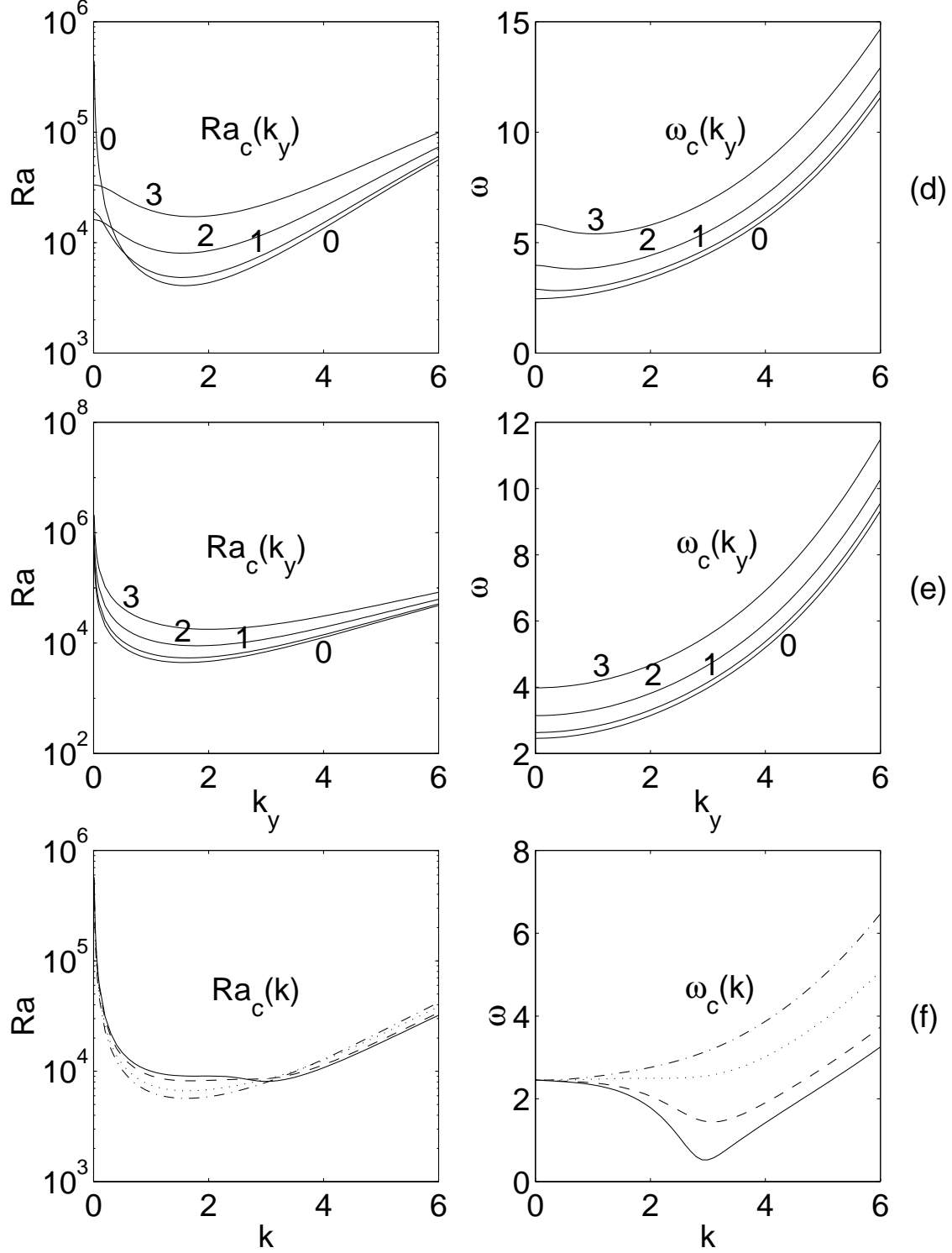


Fig. 4. Viscous fluid and stress-free slot boundaries. Curves of the marginal linear stability to 2D ($k_z = 0$) oscillatory disturbances, $Ra_c(k)$ and $\omega_c(k)$, and to such 3D ($k_z \geq 0$) disturbances with different values of k_z , $Ra_c(k_y)$ and $\omega_c(k_y)$; $\mu = 1$, $Pr = 6.7$, $Le = 1$. The numbers in (b)–(e), where the disturbances with $k_z > 0$ were also considered, give the values of k_z corresponding to their nearest curve they do not intersect. (a) $\theta = 0$; (b) $\theta = \pi/8$; (c) $\theta = \pi/4$; (d) $\theta = 3\pi/8$; (e) $\theta = \pi/2$; (f) the dash-dot lines: $\theta = 5\pi/8$, the dotted lines: $\theta = 1.35\pi/2$, the dashed lines: $\theta = 1.45\pi/2$, the solid lines: $\theta = 1.49\pi/2$.

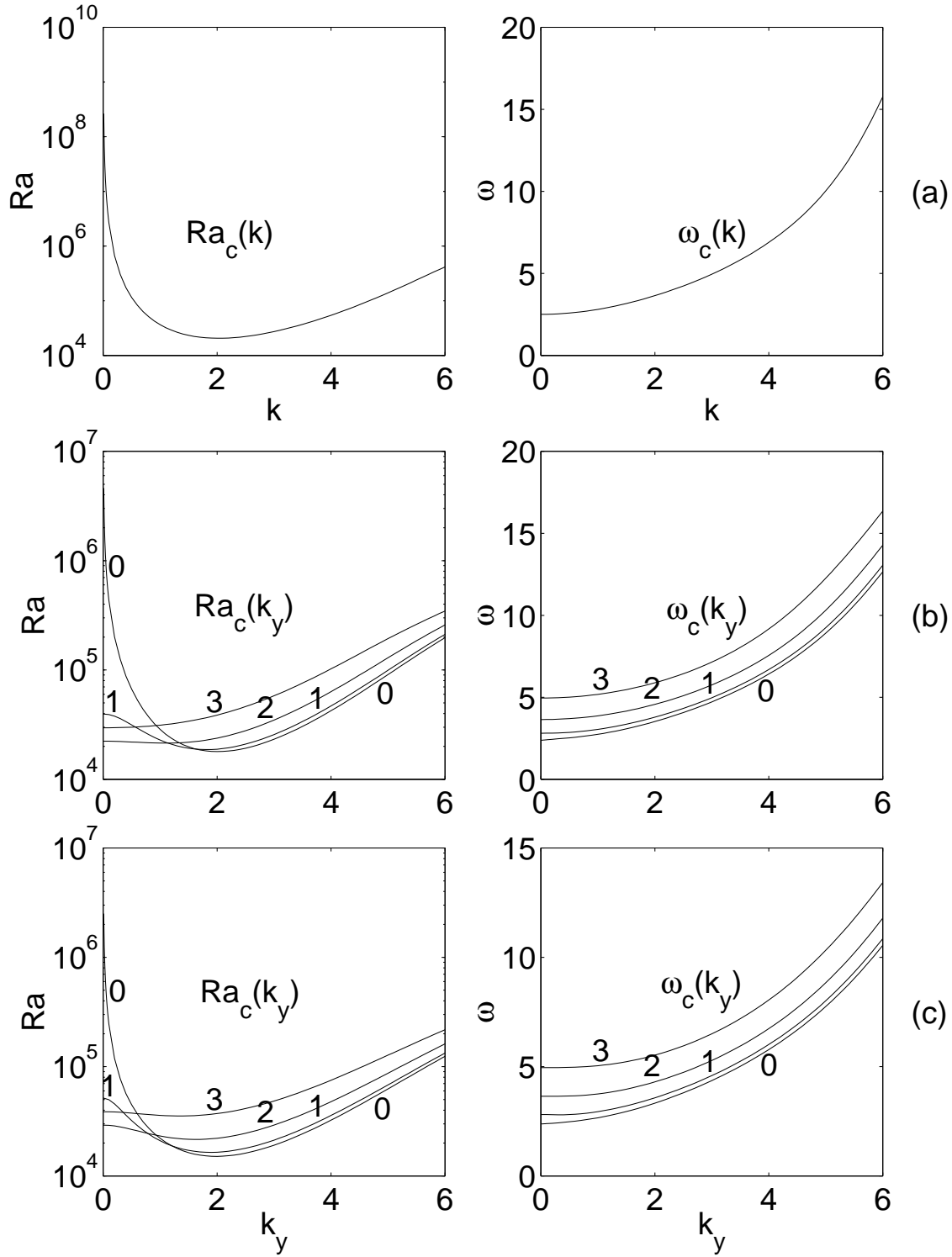


Fig. 5. Viscous fluid and no-slip slot boundaries. Curves of the marginal linear stability to 2D ($k_z = 0$) oscillatory disturbances, $Ra_c(k)$ and $\omega_c(k)$, and to such 3D ($k_z \geq 0$) disturbances with different values of k_z , $Ra_c(k_y)$ and $\omega_c(k_y)$; $\mu = 1$, $Pr = 6.7$, $Le = 1$. The numbers in (b)–(e), where the disturbances with $k_z > 0$ were also considered, give the values of k_z corresponding to their nearest curve they do not intersect. (a) $\theta = 0$; (b) $\theta = \pi/8$; (c) $\theta = \pi/4$; (d) $\theta = 3\pi/8$; (e) $\theta = \pi/2$; (f) the dash-dot lines: $\theta = 5\pi/8$, the dotted lines: $\theta = 1.3\pi/2$, the dashed lines: $\theta = 1.4\pi/2$, the solid lines: $\theta = 1.48\pi/2$.

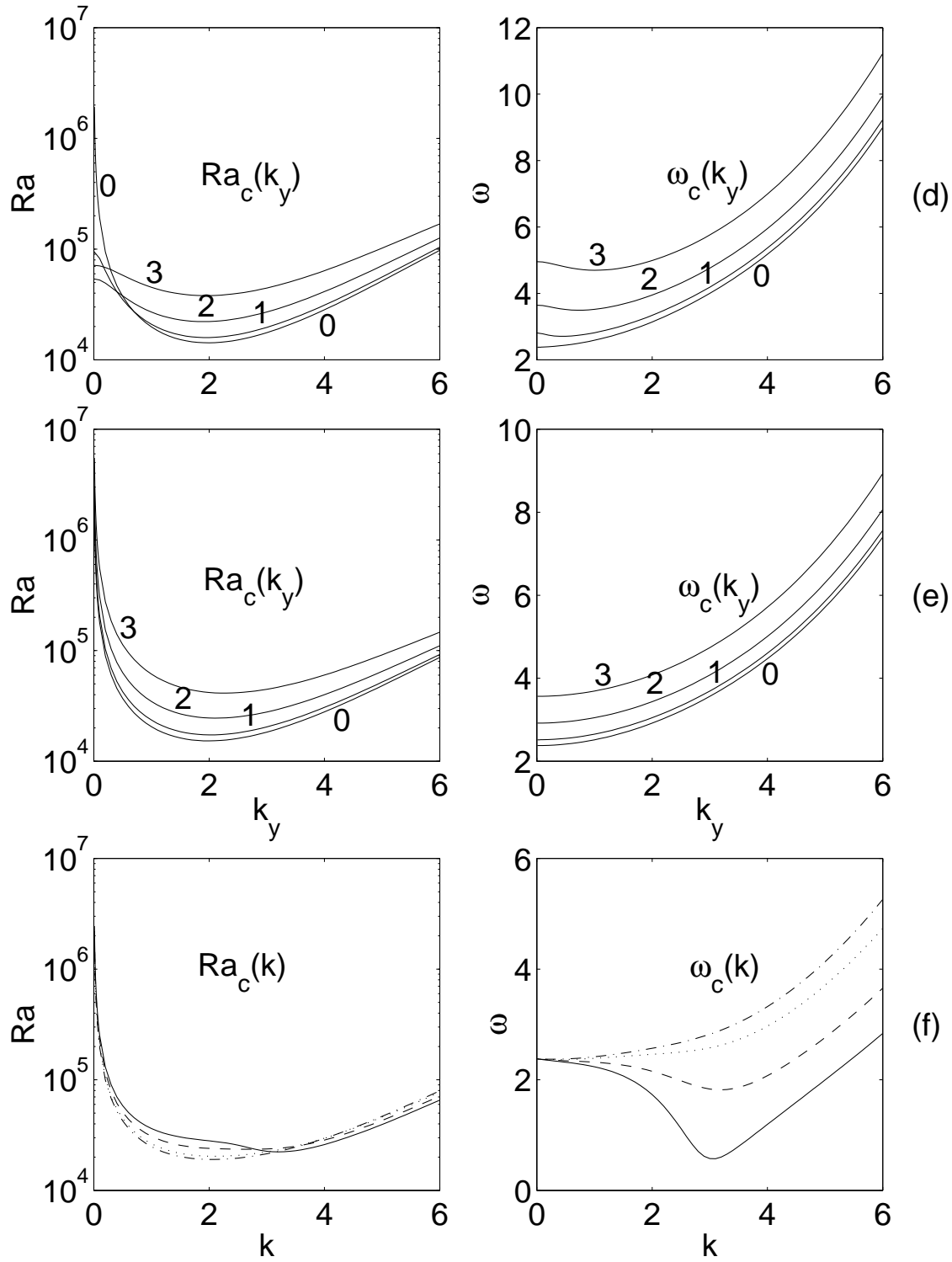


Fig. 5. Viscous fluid and no-slip slot boundaries. Curves of the marginal linear stability to 2D ($k_z = 0$) oscillatory disturbances, $Ra_c(k)$ and $\omega_c(k)$, and to such 3D ($k_z \geq 0$) disturbances with different values of k_z , $Ra_c(k_y)$ and $\omega_c(k_y)$; $\mu = 1$, $Pr = 6.7$, $Le = 1$. The numbers in (b)–(e), where the disturbances with $k_z > 0$ were also considered, give the values of k_z corresponding to their nearest curve they do not intersect. (a) $\theta = 0$; (b) $\theta = \pi/8$; (c) $\theta = \pi/4$; (d) $\theta = 3\pi/8$; (e) $\theta = \pi/2$; (f) the dash-dot lines: $\theta = 5\pi/8$, the dotted lines: $\theta = 1.3\pi/2$, the dashed lines: $\theta = 1.4\pi/2$, the solid lines: $\theta = 1.48\pi/2$.

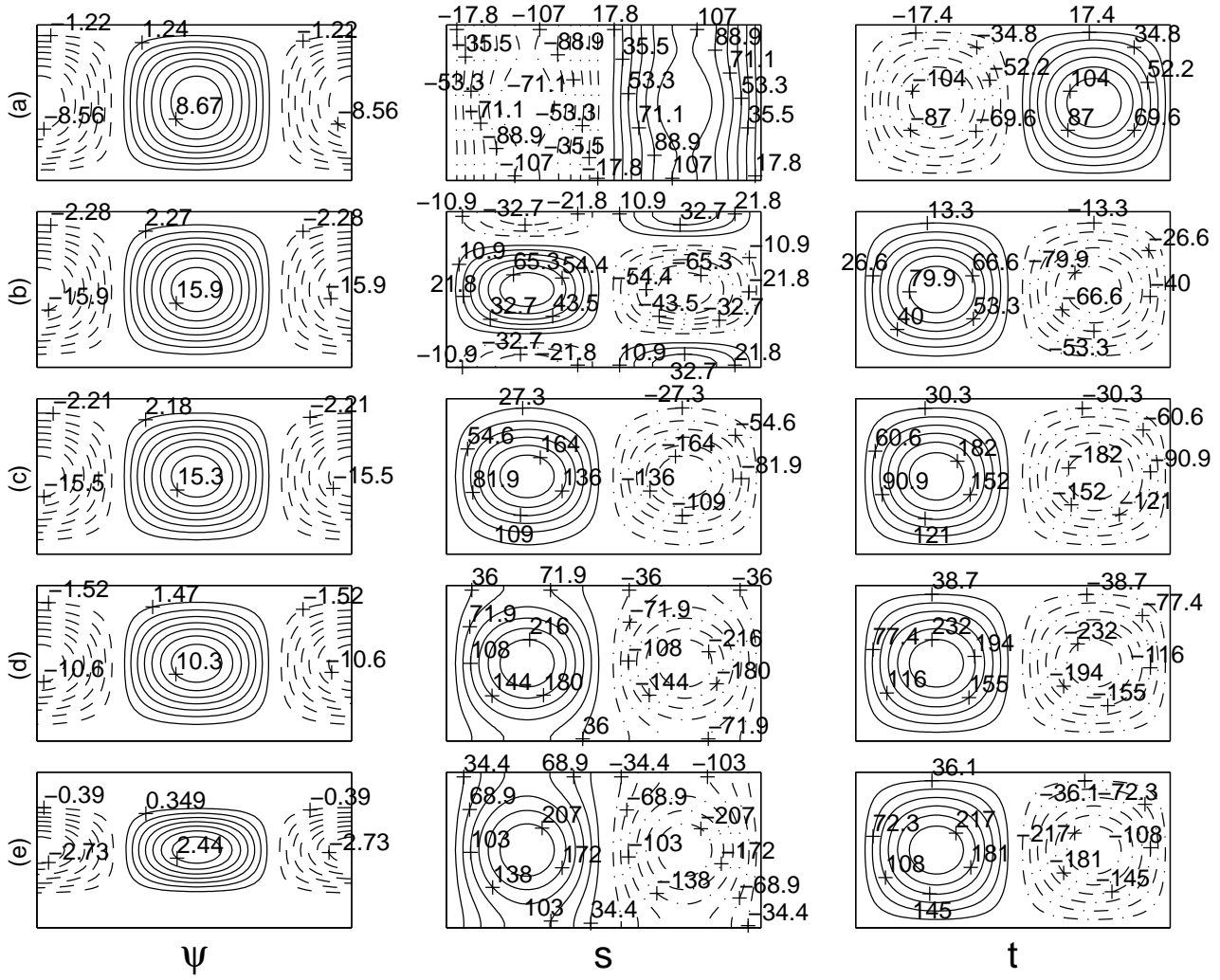


Fig. 6. $\theta = 0$. Viscous fluid and no-slip slot boundaries. Perturbation temporal behavior throughout the oscillation period $\tau_p \approx 24\delta\tau$ ($\delta\tau = 0.05$) just beyond the onset of 2D oscillatory instability. It was obtained from the numerical simulation of evolution of the linearized Eqs. (1)–(4) ($Ra_S = 0$) in response to the initial disturbance proportional to the background state after initial time $\tau_i \approx 19000$ has passed; $\lambda = 2$, $\mu = 1$, $Ra = 30060$, $Pr = 6.7$, $Le = 1$. With this τ_i , all perturbation modes other than the unstable mode ($\tau_p \approx 24\delta\tau$) are practically negligible. ψ : perturbation streamlines; s : isolines of solute concentration perturbation; t : perturbation isotherms. The actual relative values of the streamfunction perturbation are equal to 10^{-3} times the respective values in the figure. The solid and dashed streamlines designate the clockwise and counterclockwise rotation and are equally spaced within the positive and negative streamfunction intervals, respectively. The solid and dash-dot isolines of the component perturbations designate the positive and negative component perturbation intervals, respectively. (a) $\tau = \tau_i + 3\delta\tau$; (b) $\tau = \tau_i + 6\delta\tau$; (c) $\tau = \tau_i + 8\delta\tau$; (d) $\tau = \tau_i + 10\delta\tau$; (e) $\tau = \tau_i + 12\delta\tau$; (f) $\tau = \tau_i + 14\delta\tau$; (g) $\tau = \tau_i + 17\delta\tau$; (h) $\tau = \tau_i + 20\delta\tau$; (i) $\tau = \tau_i + 22\delta\tau$; (j) $\tau = \tau_i + 24\delta\tau$.

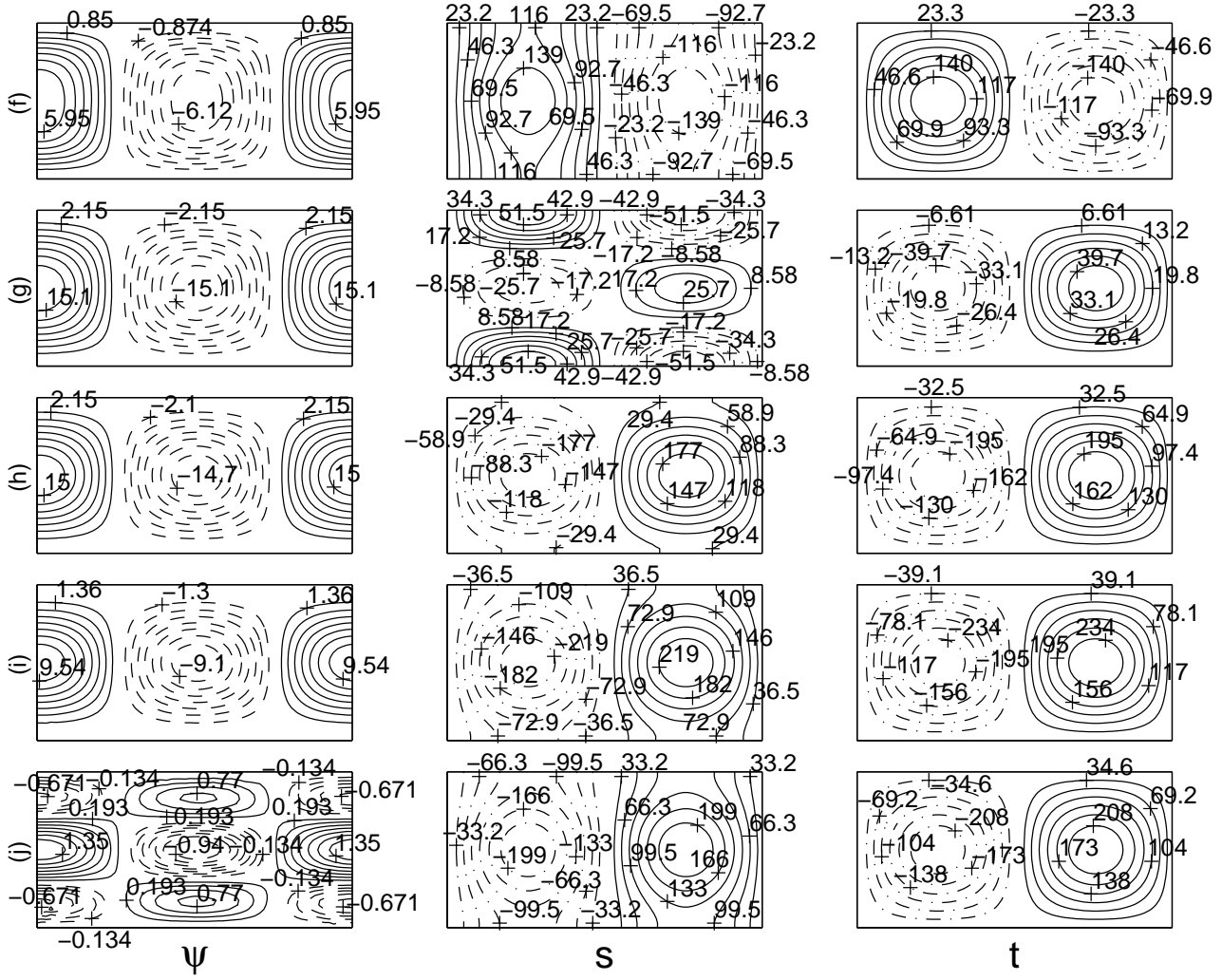


Fig. 6. $\theta = 0$. Viscous fluid and no-slip slot boundaries. Perturbation temporal behavior throughout the oscillation period $\tau_p \approx 24\delta\tau$ ($\delta\tau = 0.05$) just beyond the onset of 2D oscillatory instability. It was obtained from the numerical simulation of evolution of the linearized Eqs. (1)–(4) ($Ra_S = 0$) in response to the initial disturbance proportional to the background state after initial time $\tau_i \approx 19000$ has passed; $\lambda = 2$, $\mu = 1$, $Ra = 30060$, $Pr = 6.7$, $Le = 1$. With this τ_i , all perturbation modes other than the unstable mode ($\tau_p \approx 24\delta\tau$) are practically negligible. ψ : perturbation streamlines; s : isolines of solute concentration perturbation; t : perturbation isotherms. The actual relative values of the streamfunction perturbation are equal to 10^{-3} times the respective values in the figure. The solid and dashed streamlines designate the clockwise and counterclockwise rotation and are equally spaced within the positive and negative streamfunction intervals, respectively. The solid and dash-dot isolines of the component perturbations designate the positive and negative component perturbation intervals, respectively. (a) $\tau = \tau_i + 3\delta\tau$; (b) $\tau = \tau_i + 6\delta\tau$; (c) $\tau = \tau_i + 8\delta\tau$; (d) $\tau = \tau_i + 10\delta\tau$; (e) $\tau = \tau_i + 12\delta\tau$; (f) $\tau = \tau_i + 14\delta\tau$; (g) $\tau = \tau_i + 17\delta\tau$; (h) $\tau = \tau_i + 20\delta\tau$; (i) $\tau = \tau_i + 22\delta\tau$; (j) $\tau = \tau_i + 24\delta\tau$.

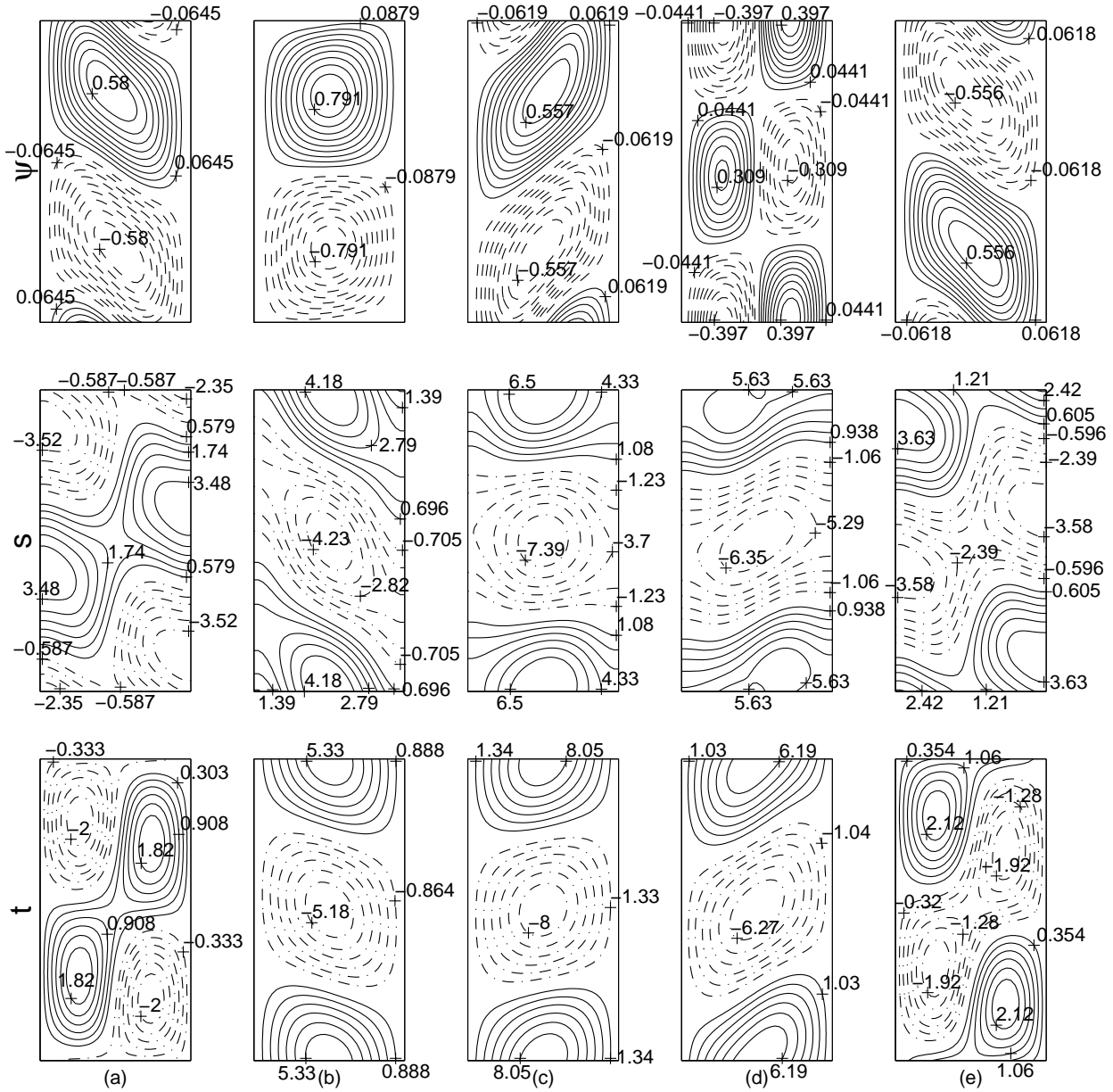


Fig. 7. $\theta = \pi/2$. Viscous fluid and no-slip slot boundaries. Perturbation temporal behavior throughout the oscillation period $\tau_p \approx 34\delta\tau$ ($\delta\tau = 0.05$) just beyond the onset of 2D oscillatory instability. It was obtained from the numerical simulation of evolution of the linearized Eqs. (1)–(4) ($Ra_S = 0$) in response to the initial disturbance proportional to the background state after initial time $\tau_i \approx 2000$ has passed; $\lambda = 2$, $\mu = 1$, $Ra = 17411$, $Pr = 6.7$, $Le = 1$. With this τ_i , all perturbation modes other than the unstable mode ($\tau_p \approx 34\delta\tau$) are practically negligible. ψ : perturbation streamlines; s : isolines of solute concentration perturbation; t : perturbation isotherms. The actual relative values of the streamfunction perturbation are equal to 10^{-3} times the respective values in the figure. The solid and dashed streamlines designate the clockwise and counterclockwise rotation and are equally spaced within the positive and negative streamfunction intervals, respectively. The solid and dash-dot isolines of the component perturbations are equally spaced within the positive and negative component perturbation intervals, respectively. (a) $\tau = \tau_i + 3\delta\tau$; (b) $\tau = \tau_i + 7\delta\tau$; (c) $\tau = \tau_i + 11\delta\tau$; (d) $\tau = \tau_i + 15\delta\tau$; (e) $\tau = \tau_i + 19\delta\tau$; (f) $\tau = \tau_i + 22\delta\tau$; (g) $\tau = \tau_i + 25\delta\tau$; (h) $\tau = \tau_i + 28\delta\tau$; (i) $\tau = \tau_i + 31\delta\tau$; (j) $\tau = \tau_i + 34\delta\tau$.

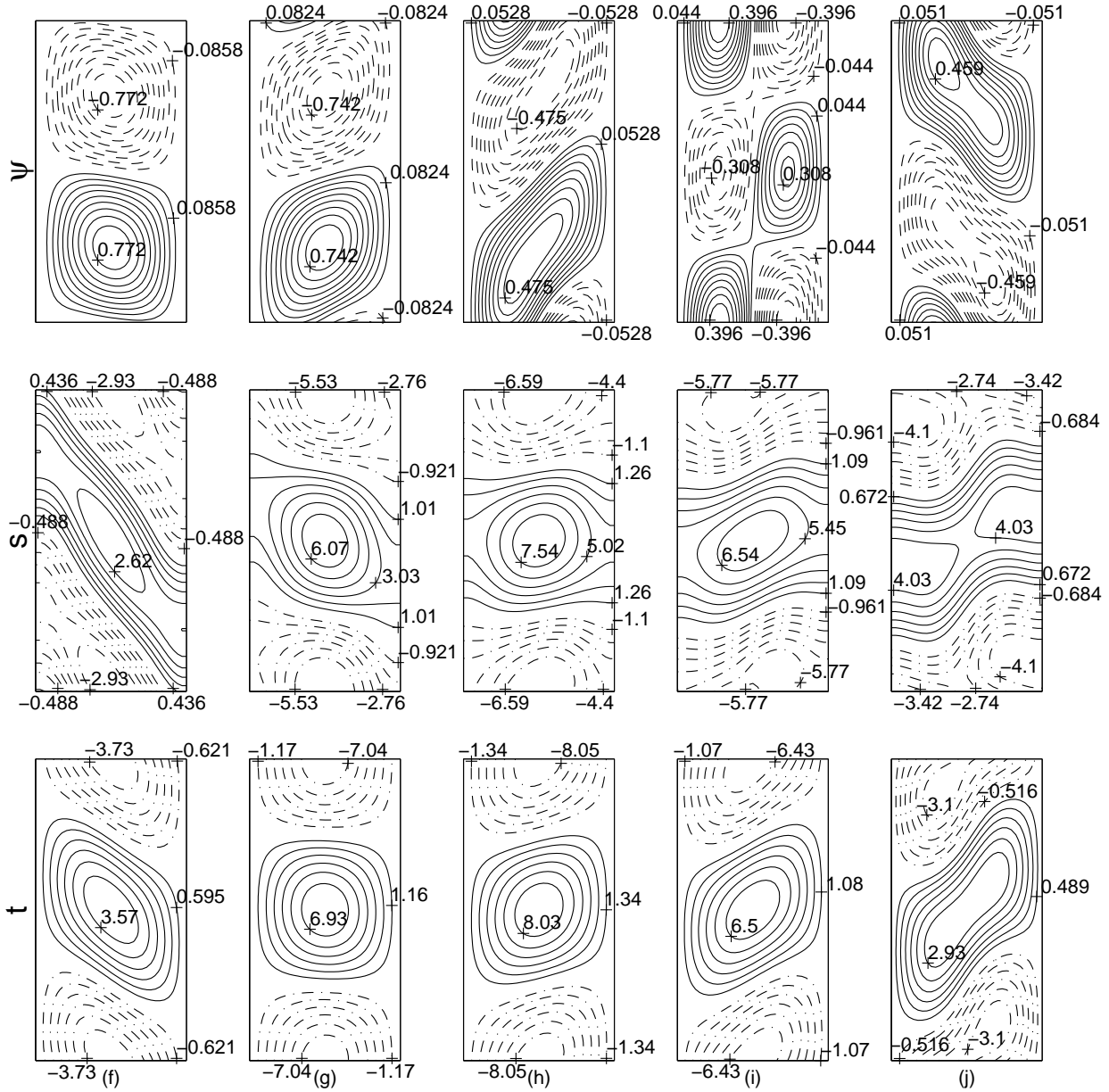


Fig. 7. $\theta = \pi/2$. Viscous fluid and no-slip slot boundaries. Perturbation temporal behavior throughout the oscillation period $\tau_p \approx 34\delta\tau$ ($\delta\tau = 0.05$) just beyond the onset of 2D oscillatory instability. It was obtained from the numerical simulation of evolution of the linearized Eqs. (1)–(4) ($Ra_S = 0$) in response to the initial disturbance proportional to the background state after initial time $\tau_i \approx 2000$ has passed; $\lambda = 2$, $\mu = 1$, $Ra = 17411$, $Pr = 6.7$, $Le = 1$. With this τ_i , all perturbation modes other than the unstable mode ($\tau_p \approx 34\delta\tau$) are practically negligible. ψ : perturbation streamlines; s : isolines of solute concentration perturbation; t : perturbation isotherms. The actual relative values of the streamfunction perturbation are equal to 10^{-3} times the respective values in the figure. The solid and dashed streamlines designate the clockwise and counterclockwise rotation and are equally spaced within the positive and negative streamfunction intervals, respectively. The solid and dash-dot isolines of the component perturbations are equally spaced within the positive and negative component perturbation intervals, respectively. (a) $\tau = \tau_i + 3\delta\tau$; (b) $\tau = \tau_i + 7\delta\tau$; (c) $\tau = \tau_i + 11\delta\tau$; (d) $\tau = \tau_i + 15\delta\tau$; (e) $\tau = \tau_i + 19\delta\tau$; (f) $\tau = \tau_i + 22\delta\tau$; (g) $\tau = \tau_i + 25\delta\tau$; (h) $\tau = \tau_i + 28\delta\tau$; (i) $\tau = \tau_i + 31\delta\tau$; (j) $\tau = \tau_i + 34\delta\tau$.

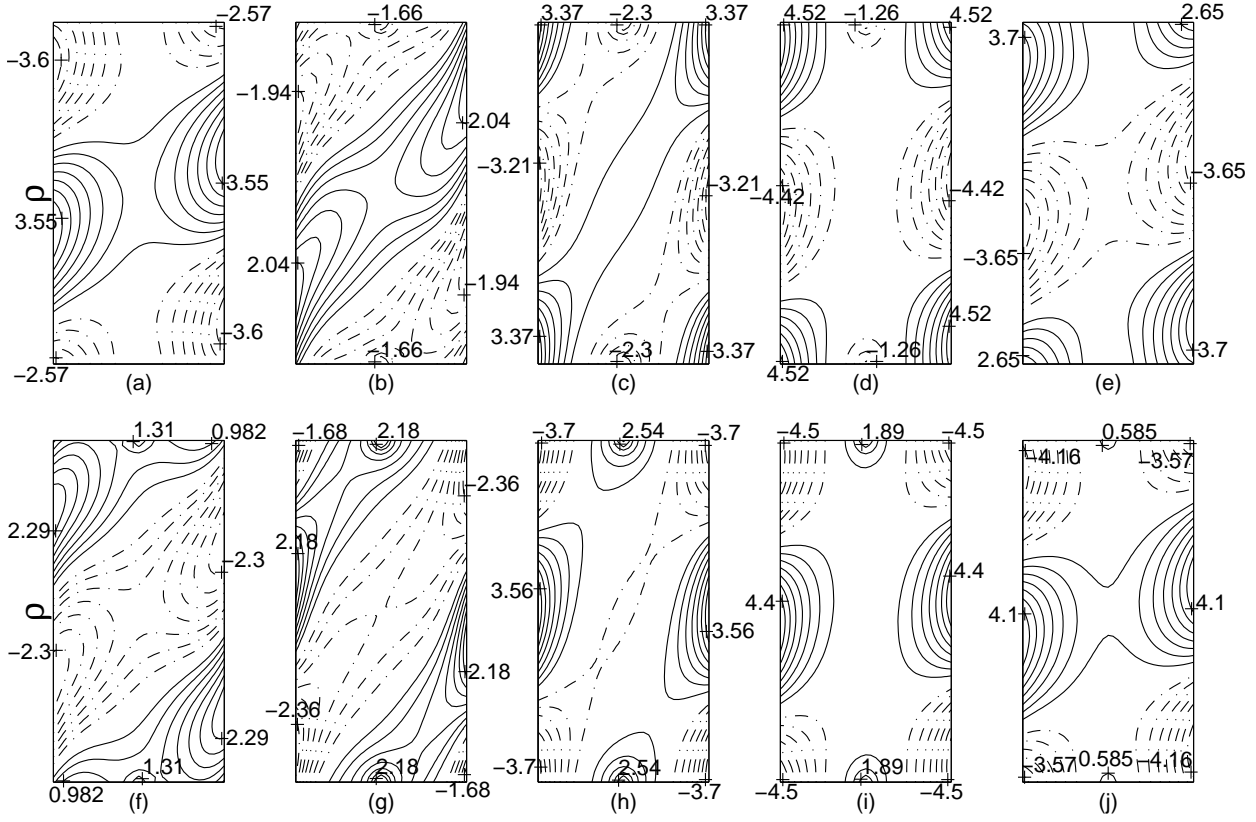


Fig. 8. The same as in Fig. 7. ρ : isolines of the perturbation in $s - t$. The solid and dash-dot isolines are equally spaced within the positive and negative density perturbation intervals, respectively.

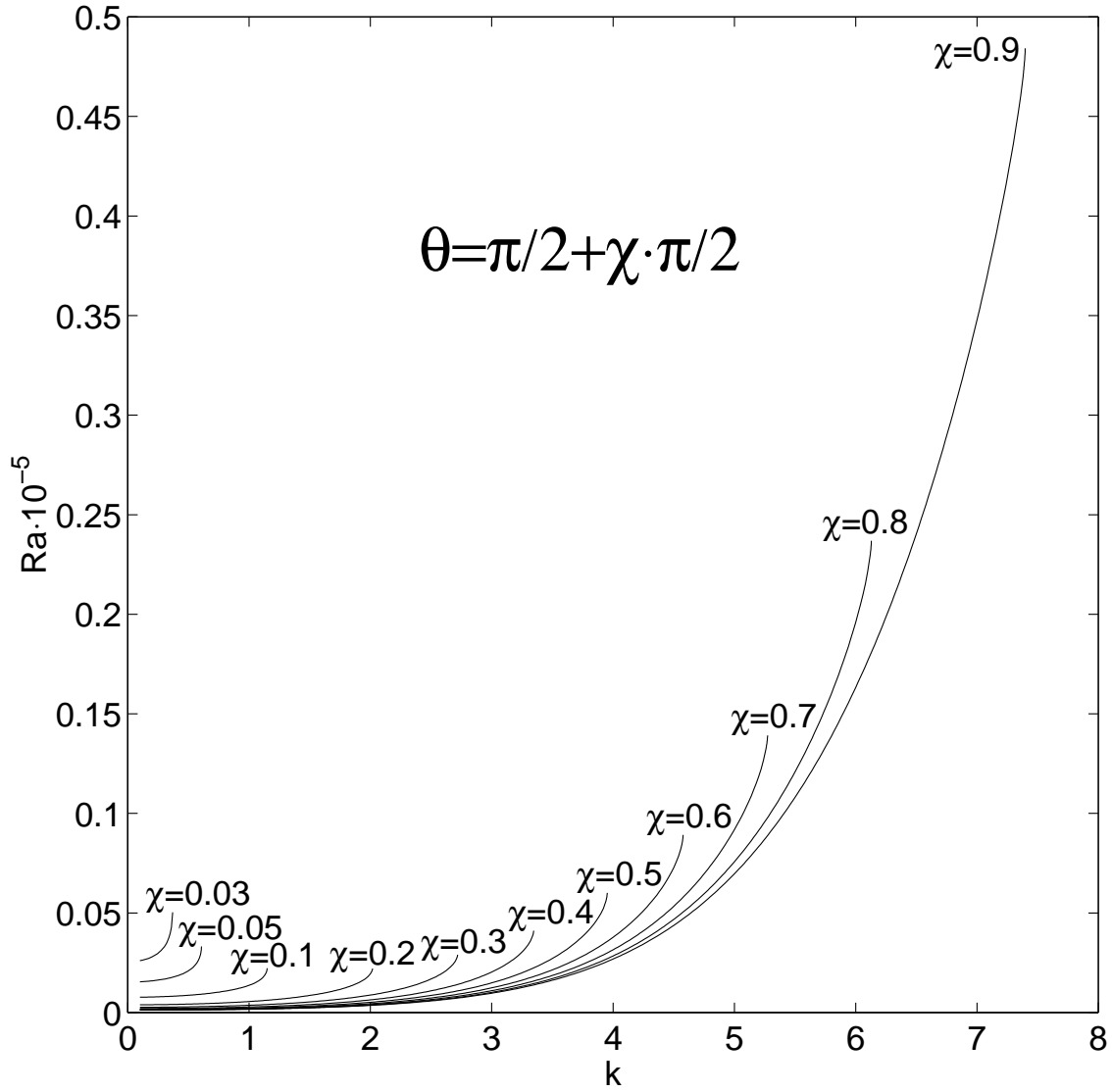


Fig. 9. Viscous fluid and stress-free slot boundaries. Curves of the marginal linear stability to 2D steady disturbances, $Ra_c(k)$, for different $\theta = (1 + \chi)\pi/2$, $0 < \chi < 1$; $\mu = 1$, $Le = 1$. The data for the wave numbers very close to $k = 0$ (where stable data were numerically difficult to obtain) are not presented.

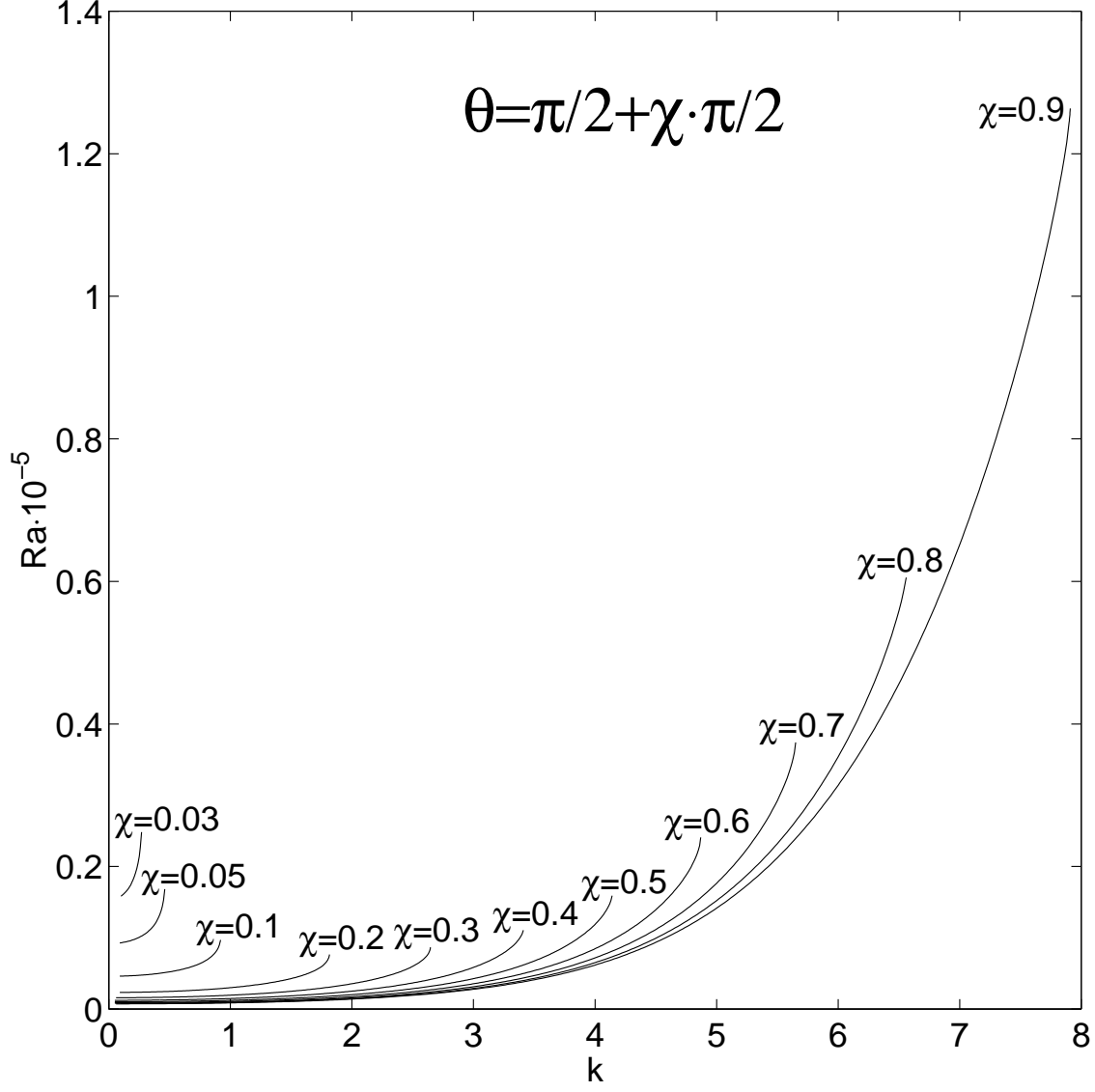


Fig. 10. Viscous fluid and no-slip slot boundaries. Curves of the marginal linear stability to 2D steady disturbances, $Ra_c(k)$, for different $\theta = (1 + \chi)\pi/2$, $0 < \chi < 1$; $\mu = 1$, $Le = 1$. The data for the wave numbers very close to $k = 0$ (where stable data were numerically difficult to obtain) are not presented.

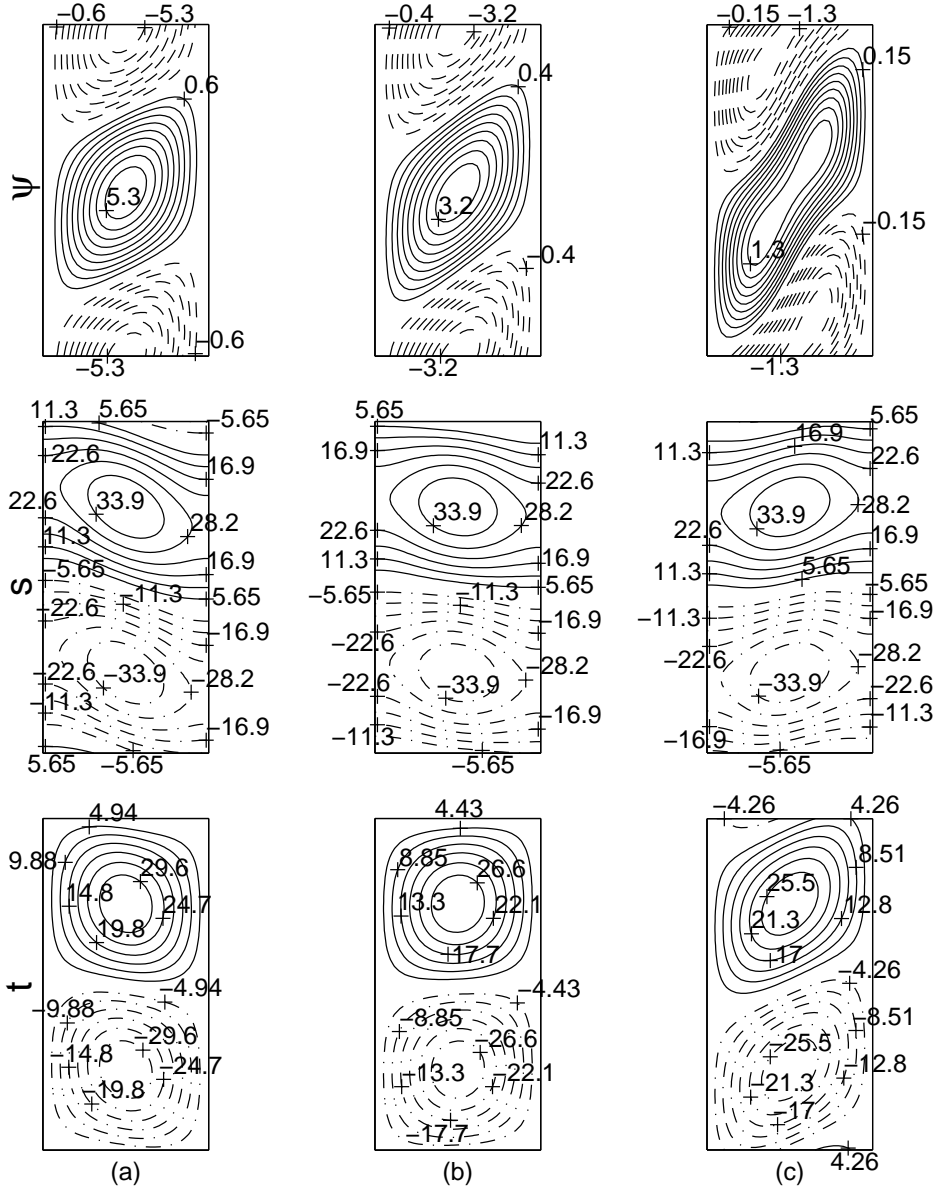


Fig. 11. $\theta = \pi/2$. Viscous fluid and no-slip slot boundaries. Singular eigenvectors corresponding to the wavelength $\lambda = 2$ at the onset of small-amplitude steady convection within a narrow interval of μ where the linear steady instability for $\lambda = 2$ arises; $Pr = 6.7$, $Le = 1$. ψ : perturbation streamlines; s : isolines of solute concentration perturbation; t : perturbation isotherms. The variables are nondimensionalized as in Eqs. (1)–(4) ($Ra_S = 0$). The actual relative values of the streamfunction perturbation are equal to 10^{-3} times the respective values in the figure. The solid and dashed streamlines designate the clockwise and counterclockwise rotation and are equally spaced within the positive and negative streamfunction perturbation intervals, respectively. The solid and dash-dot isolines of the component perturbations designate the positive and negative component perturbation intervals, respectively. (a) $\mu = 0.92$, $Ra_c = 6139$; (b) $\mu = 0.96$, $Ra_c = 8900$; (c) $\mu = 0.98$, $Ra_c = 22469$.

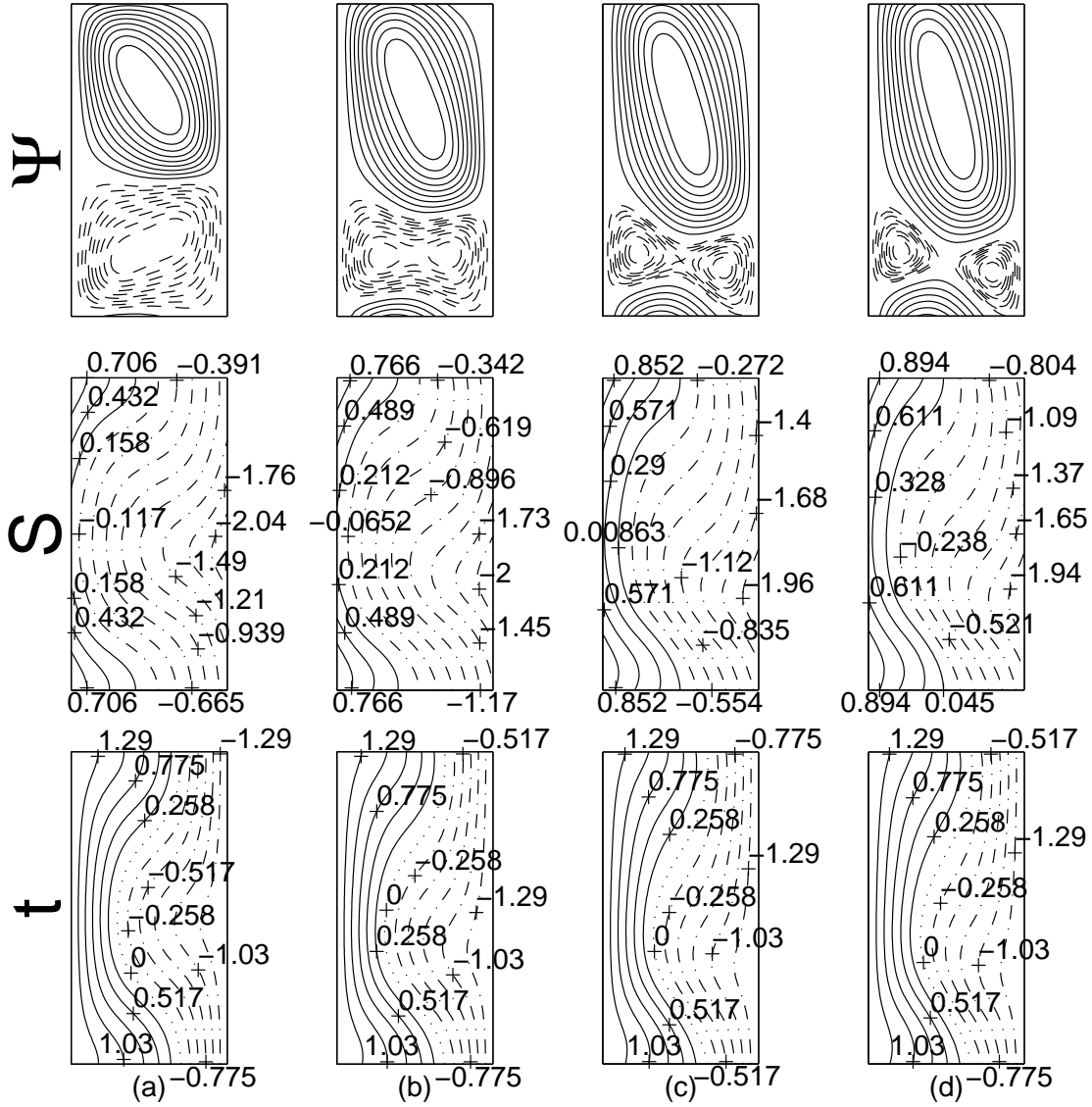


Fig. 12. Viscous fluid and no-slip slot boundaries. Finite-amplitude convective steady flows representing the higher-amplitude branch, $A2$, for different $\theta \in (\pi/2, \pi)$; $\lambda = 2$, $\mu = 1$, $Ra = 31000$, $Pr = 6.7$, $Le = 1$. The steady solutions were obtained from Eqs. (1)–(4) ($Ra_S = 0$). The across- and along-slot coordinate axes are directed rightwards and upwards, respectively. Ψ : streamlines; S : isolines of solute concentration; t : isotherms. The actual values of t and s are equal to 10^4 times the respective values in the figure. The solid and dashed streamlines designate the clockwise and counterclockwise rotation and are equally spaced within the positive and negative streamfunction intervals, respectively. The solid and dash-dot component isolines designate the positive and negative component values, respectively. The zero isotherms are designated by the dotted lines. (a) $\theta = 1.99\pi/2$; (b) $\theta = 1.97\pi/2$; (c) $\theta = 1.95\pi/2$; (d) $\theta = 1.94\pi/2$; (e) $\theta = 1.9\pi/2$; (f) $\theta = 1.75\pi/2$; (g) $\theta = 1.7\pi/2$; (h) $\theta = 1.1\pi/2$.

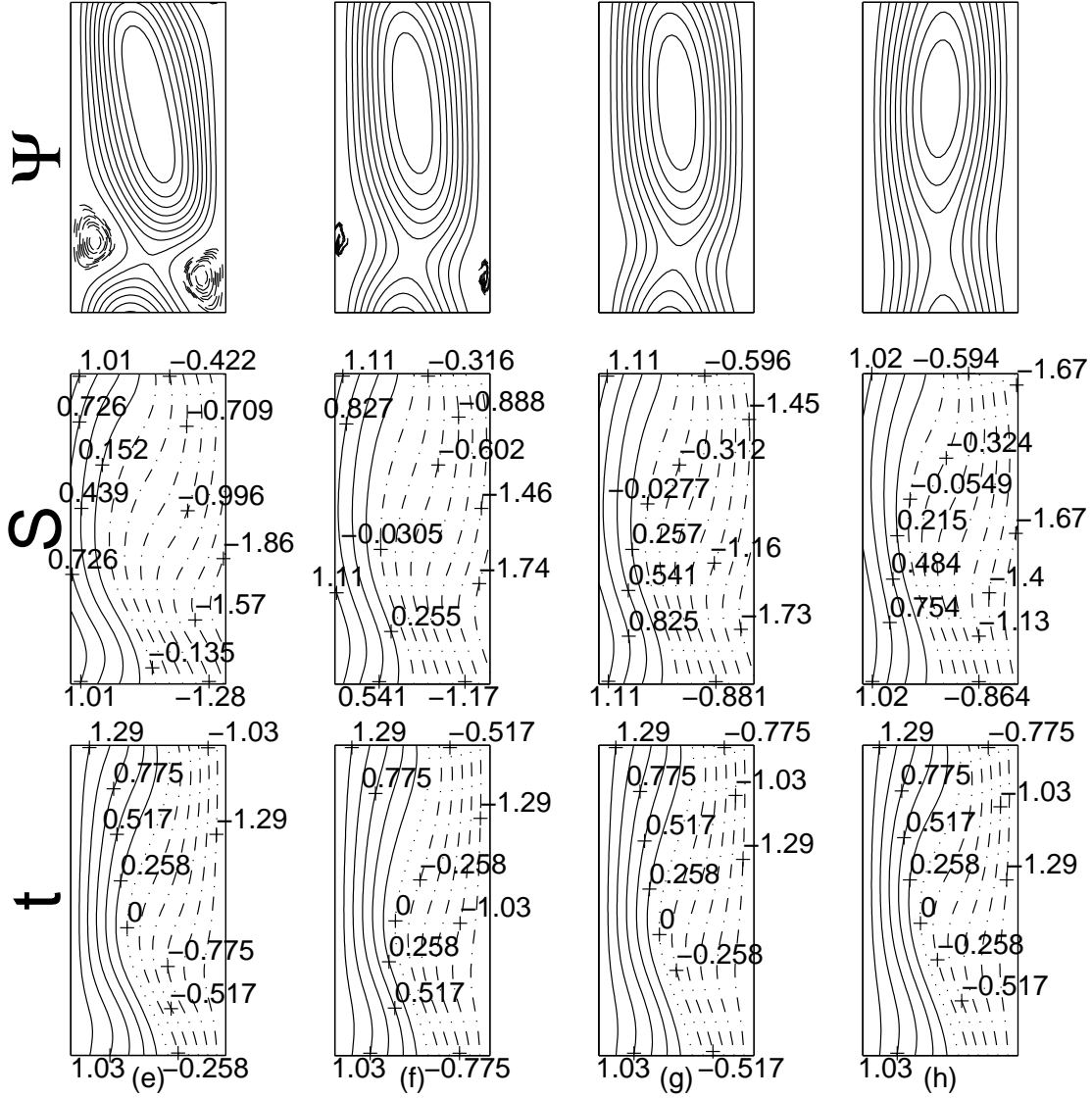


Fig. 12. Viscous fluid and no-slip slot boundaries. Finite-amplitude convective steady flows representing the higher-amplitude branch, $A2$, for different $\theta \in (\pi/2, \pi)$; $\lambda = 2$, $\mu = 1$, $Ra = 31000$, $Pr = 6.7$, $Le = 1$. The steady solutions were obtained from Eqs. (1)–(4) ($Ra_S = 0$). The across- and along-slot coordinate axes are directed rightwards and upwards, respectively. Ψ : streamlines; S : isolines of solute concentration; t : isotherms. The actual values of t and s are equal to 10^4 times the respective values in the figure. The solid and dashed streamlines designate the clockwise and counterclockwise rotation and are equally spaced within the positive and negative streamfunction intervals, respectively. The solid and dash-dot component isolines designate the positive and negative component values, respectively. The zero isotherms are designated by the dotted lines. (a) $\theta = 1.99\pi/2$; (b) $\theta = 1.97\pi/2$; (c) $\theta = 1.95\pi/2$; (d) $\theta = 1.94\pi/2$; (e) $\theta = 1.9\pi/2$; (f) $\theta = 1.75\pi/2$; (g) $\theta = 1.7\pi/2$; (h) $\theta = 1.1\pi/2$.

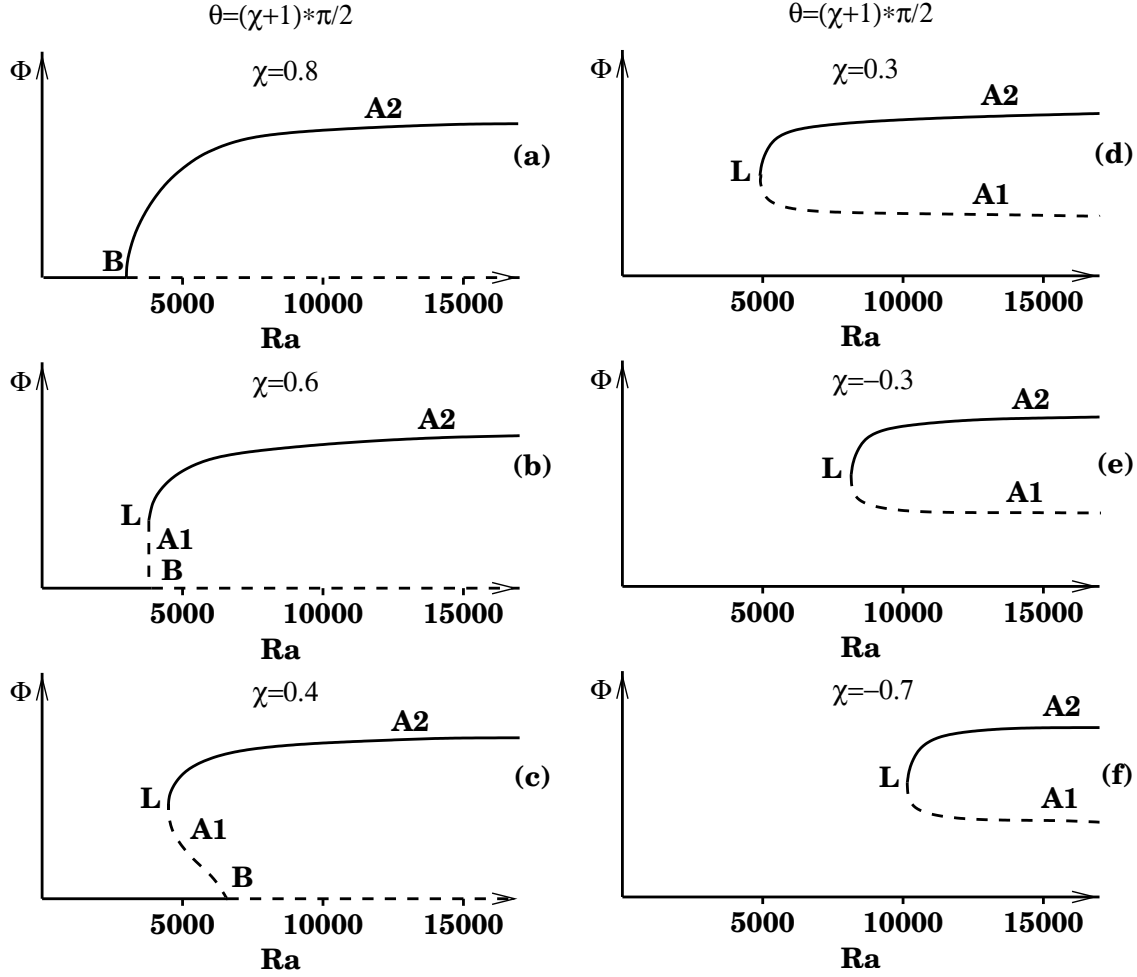


Fig. 13. Viscous fluid and no-slip slot boundaries. Schematic diagrams illustrating structures of the steady flows representing onset of the linear and finite-amplitude steady instability of the conduction state as Ra is increased for different $\theta = (\chi + 1)\pi/2$, $-1 < \chi < 1$; $\lambda = 2$, $\mu = 1$, $Pr = 6.7$, $Le = 1$. Φ is an abstract measure of the steady flows that distinguishes between different steady solutions, specifies the location of the singularities (limit points and symmetry-breaking bifurcations), and represents the flows arising from a symmetry-breaking bifurcation as a single branch. The solid (dashed) lines represent the branches expected to be linearly stable (unstable) to the disturbances associated with the eigenvalues that give rise to the steady instability of the conduction state. Secondary oscillatory and steady bifurcations, if any, are not shown. B is the symmetry-breaking bifurcation standing for the steady linear stability boundary for wave number $k = \pi$ ($\lambda = 2$). L is the limit point. $A1$ and $A2$ are the lower- and higher-amplitude branches associated with the limit point, respectively. (a) $\theta = 1.8\pi/2$; (b) $\theta = 1.6\pi/2$; (c) $\theta = 1.4\pi/2$; (d) $\theta = 1.3\pi/2$; (e) $\theta = 0.7\pi/2$; (f) $\theta = 0.3\pi/2$.

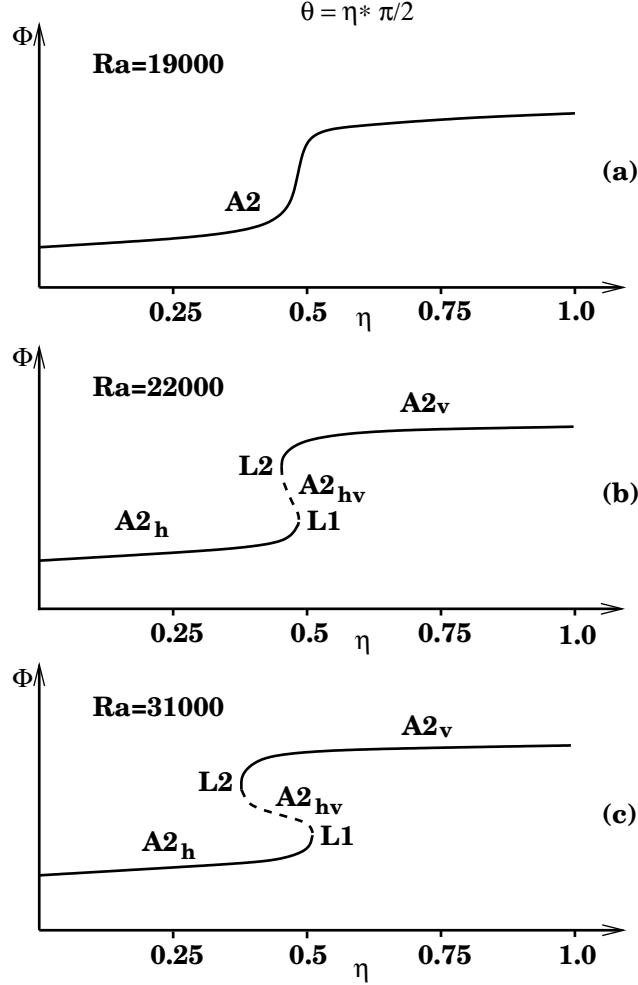


Fig. 14. Viscous fluid and no-slip slot boundaries. Schematic diagrams illustrating structures of the steady flows of the higher-amplitude convective branch, $A2$, with the minimal along-slot period $\lambda = 2$ as $\theta = \eta\pi/2$ is varied for different Ra , $\eta \in [0, 1]$; $\mu = 1$, $Pr = 6.7$, $Le = 1$. Φ is an abstract measure of the steady flows that distinguishes between different steady solutions and specifies the location of the singularities (limit points). The dashed lines imply that the respective branches are linearly unstable to steady disturbances. $A2_h$ and $A2_v$ are the convective branches continuously transformed into the higher-amplitude branches in the horizontal and vertical slot, respectively. $A2_{hv}$ is the linearly unstable (to steady disturbances) branch connecting branches $A2_h$ and $A2_v$ via limit points $L1$ and $L2$. Secondary instability, if any, of the depicted steady branches to the oscillatory and steady disturbances other than the (steady) disturbances destabilizing branch $A2_{hv}$ is not shown. (a) $Ra = 19000$; (b) $Ra = 22000$; (c) $Ra = 31000$.

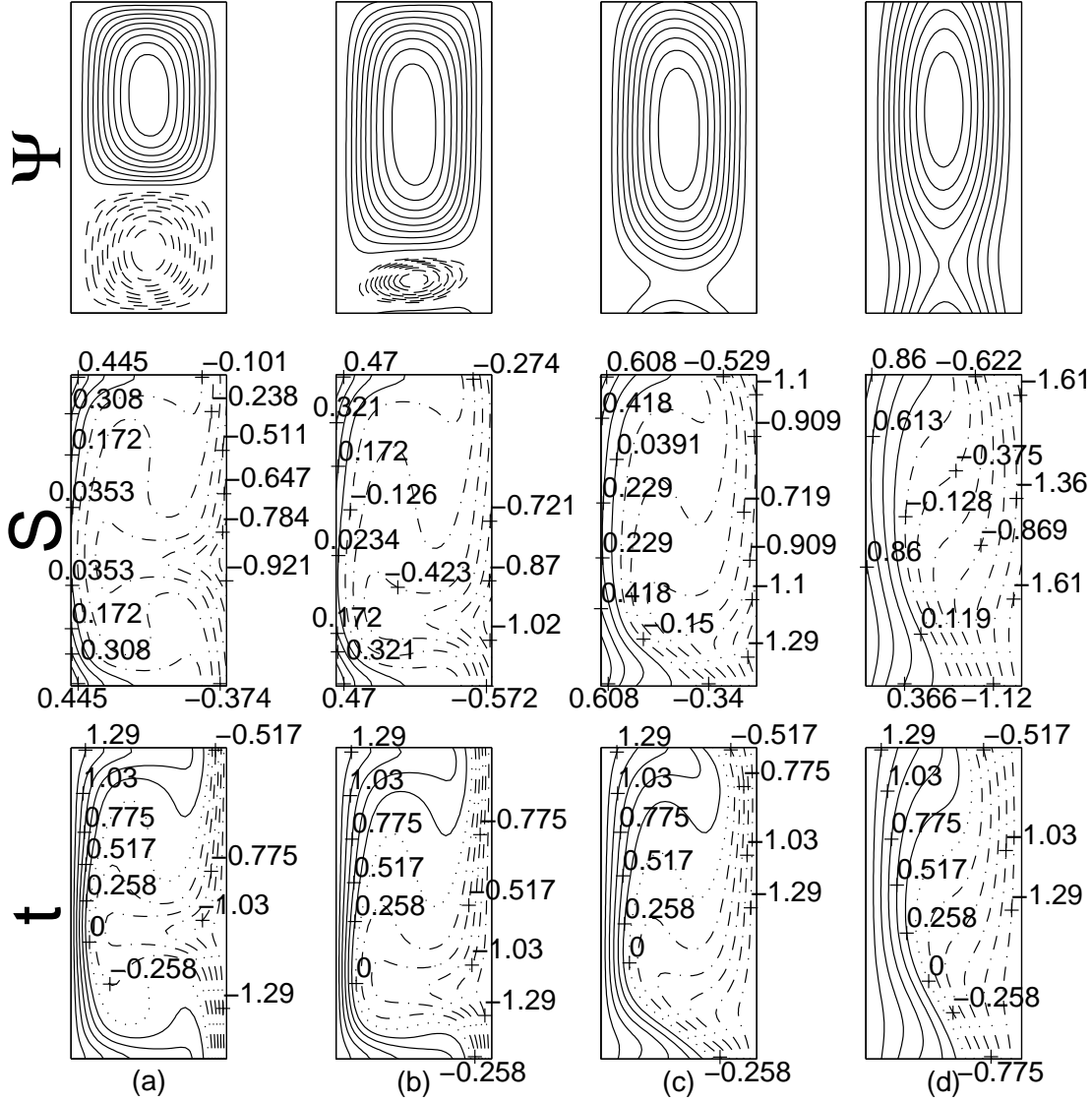


Fig. 15. Viscous fluid and no-slip slot boundaries. Finite-amplitude convective steady flows representing the higher-amplitude branch, $A2$, for different $\theta \in (0, \pi/2)$; $\lambda = 2$, $\mu = 1$, $Ra = 31000$, $Pr = 6.7$, $Le = 1$. The steady solutions were obtained from Eqs. (1)–(4) ($Ra_S = 0$). The across- and along-slot coordinate axes are directed rightwards and upwards, respectively. Ψ : streamlines; S : isolines of solute concentration; t : isotherms. The actual values of t and s are equal to 10^4 times the respective values in the figure. The solid and dashed streamlines designate the clockwise and counterclockwise rotation and are equally spaced within the positive and negative streamfunction intervals, respectively. The solid and dash-dot component isolines designate the positive and negative component values, respectively. The zero isotherms are designated by the dotted lines. (a) $\theta = 0.2\pi/2$, branch $A2_h$; (b) $\theta = 0.5\pi/2$, branch $A2_{hv}$; (c) $\theta = 0.4\pi/2$, branch $A2_{hv}$; (d) $\theta = 0.5\pi/2$, branch $A2_v$.